Portland State University

PDXScholar

8-3-2020

Synthesis and Assessment of Radiotherapy-Enhancing Nanoparticles

Hayden Winter
Portland State University

Follow this and additional works at: https://pdxscholar.library.pdx.edu/open_access_etds

Part of the Inorganic Chemistry Commons, and the Nanoscience and Nanotechnology Commons

Let us know how access to this document benefits you.

Synthesis and Assessment of Radiotherapy-Enhancing Nanoparticles

by

Hayden Winter

A dissertation submitted in partial fulfillment of the
requirements for the degree of

Doctor of Philosophy
in
Chemistry

Dissertation Committee:
Andrea Goforth, Chair
David Stuart
Mark Woods
Ralf Widenhorn

Portland State University
2020

Abstract

Radiation Therapy (RT) is a common treatment for cancerous lesions that acts by ionizing matter in the affected tissue, causing cell death. The disadvantage of RT is that it is most often delivered via an external beam of radiation which must pass through healthy tissues to reach the target site, ionizing matter within healthy tissues as well. To address this drawback, techniques are being developed for increasing RT-induced cell death in a target tissue while minimizing cell death in surrounding tissues. This effect is known as radiation dose enhancement or RT enhancement.

The approach to RT enhancement studied in this thesis involves the use of inorganic nanoparticles (NPs) within target cells. Theses NPs attenuate X-ray radiation more effectively than the tissues around them, thus depositing more energy into the target tissue. This enhanced energy deposition in the target tissue allows a lesser dose of radiation to be applied to effectively treat the target tissue, which may reduce the risk of cell damage in the surrounding healthy tissues.

In this thesis, the synthesis of two types of RT-enhancing NPs was studied, and preliminary biological assays were used to assess their effectiveness *in vitro*.

First, a novel synthesis of bismuth nanoparticles (Bi NPs) was developed. Bi NPs are promising RT enhancers due to their high density and atomic number, properties that increase X-ray attenuation. However, syntheses of Bi NPs necessitate air-free technique and specialized equipment. The presented synthesis is aerobic and only uses standard laboratory equipment, providing a practical synthesis that produces Bi NPs of an

appropriate size for RT enhancement applications. This is possible due to the formation of an iodobismuthate precursor which is rapidly reduced to form metallic bismuth, eliminating the need for air and light-sensitive bismuth precursors. A survey of the parameters of the reaction has illustrated the impact of various factors to guide further optimization or reproduction of the synthesis. After synthesizing Bi NPs, they were then covered in a silica shell which enabled their further modification in aqueous media.

Second, CaF_2:Ln NPs were synthesized and incorporated into an RT enhancing NP which was also radioluminescent (RL). Along with RT enhancement via X-ray scattering, these NPs may enable RL imaging and deep-tissue photodynamic therapy. This work includes a rarely found time point study which elucidates the mechanism by which annealing at high pressure corrects crystalline defects improves their luminescence intensity. The CaF_2 NPs were then coated in a mesoporous silica shell which allowed for further surface modification as well as small molecule loading. This shell was then further modified with polyethylene glycol, rendering the NP highly stable in water and lessening the chance of immune response.

Lastly, with both NP types completely synthesized, a variety of biological assays were performed to assess their effectiveness in RT enhancement. Fluorescent probes were used to determine that the presence of NPs increases the number of reactive oxygen species formed during RT, which can be correlated to cell death. *In vitro* experiments were performed with variable doses of NPs and X-ray radiation to assess the NPs effectiveness at enhancing RT. Finally, an *in vivo* experiment is reported which supported that the Bi NPs are biodegradable when injected intravenously. These biological assays presented

evidence of RT enhancement for both types of NPs in this thesis and directed future work to address some shortcomings in cytocompatibility and reactive oxygen species generation.

Graphic Outline of Nanoparticle Synthesis in this Thesis
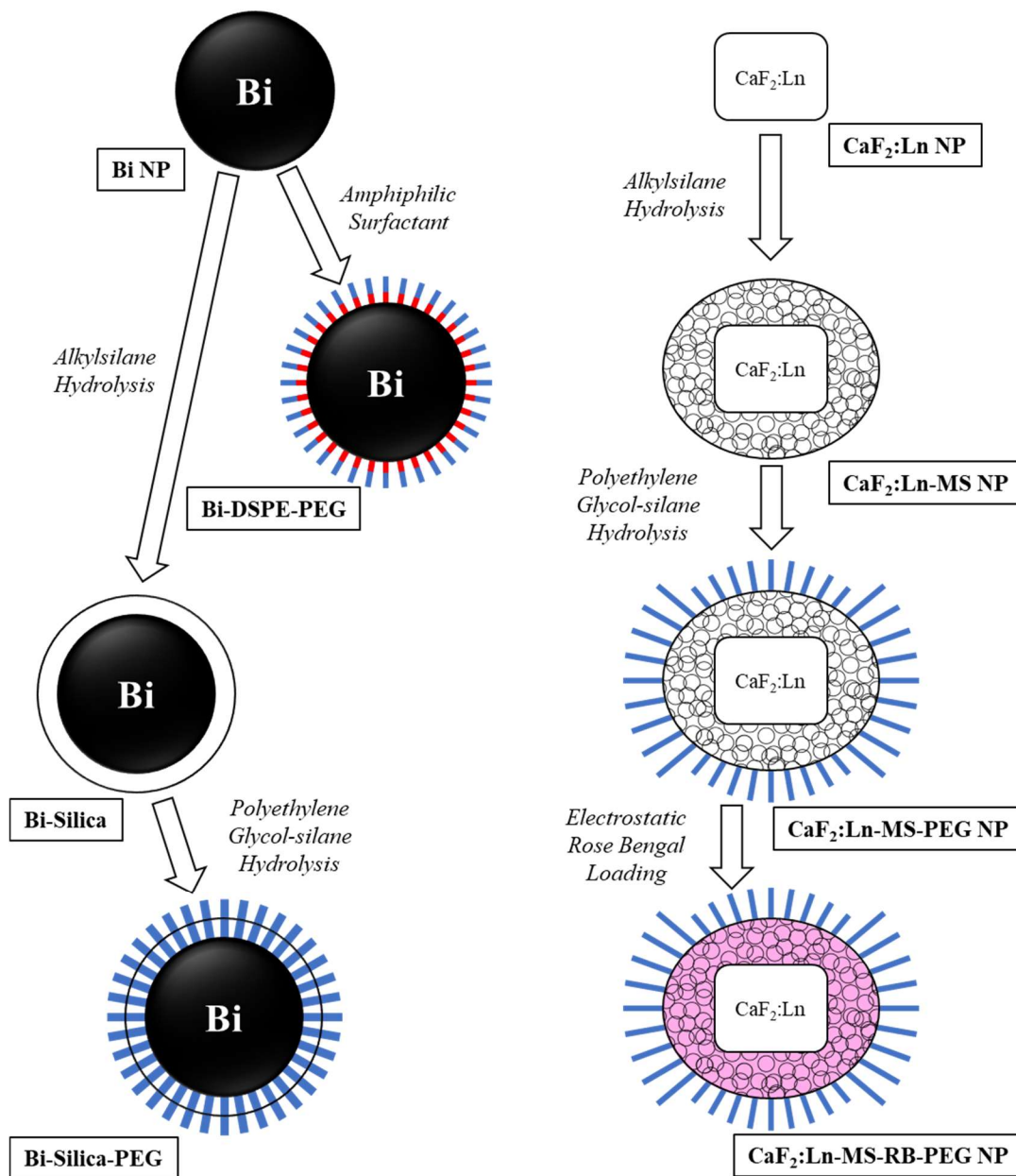
Dedication

This thesis is dedicated to my Mom and Dad, who gave me every last bit of support they ever could, and still continue to. I love you both!

Acknowledgments

Table of Contents

List of Tables

List of Figures

List of Equations

List of Schemes

CHAPTER 1 - INTRODUCTION TO RADIOTHERAPY AND X-RAY-MATTER

INTERACTIONS

1.1. X-ray Radiotherapy

X-ray radiotherapy (RT) is a common treatment for the management of cancerous lesions. RT can be used alone, used to enhance the effects of chemotherapy, or used before or after tumor resection to lessen the risk of tumor resurgence. In 2015, 490,000 Americans received RT, with that number forecasted to increase by 19% to 580,000 by 2025.[1] In most cases of X-ray RT, the patient is positioned on a bed below a linear accelerator (LINAC) that serves as the source of radiation. The LINAC produces a fine beam of X-ray radiation on the MeV scale, which provides a predictable and homogenous path of radiation. Intensity Modulated Radiotherapy is most often used, in which the patient is exposed to the radiation in a highly controlled manner that maximizes exposure to the cancerous tissue while minimizing exposure to healthy tissues.[2] This can be done by rotating the radiation source or the patient, as well as with the use of radiation shielding materials over healthy

tissues. By rotating the patient or radiation source around an axis containing the cancerous tissue, it is continuously exposed to radiation while the healthy tissue around it is only briefly exposed. In addition to these techniques, the latest research indicates that fractionating radiation doses over several visits leads to a greater tumor volume reduction, as well as lessened side effects.[2]

Even with these considerations, some limitations are innate to RT as it is performed today. The most detrimental issue is the limited control of dose deposition, or determination of what tissues are irradiated. To treat a tumor, a beam of ionizing radiation must be fired through healthy tissue around the tumor, and any photons that transmit through the tumor tissue will pass through the healthy tissue on the other side of the tumor. The radiation dose deposited into the healthy tissue around the tumor can damage it and prevent it from functioning properly. Worse still, ionization of DNA in healthy tissues may cause mutations that lead to secondary carcinogenesis. This limitation has been shown to have significant effects on the outcome of patients who receive RT. Studies of these phenomena are often separated by the location of tumors, as this determines which types of healthy tissues are affected during RT. One such study of breast cancer patients found that while 13% of patients who received RT and were later diagnosed with secondary carcinomas, 3.4% of the total studied population could attribute the appearance of secondary carcinoma to RT.[3] A large study of colorectal cancer patients showed that RT increased the risk of secondary carcinomas, most often endometrial, lung, and bladder cancer as well as lymphomas.[4] Due to this issue, there are a variety of methods being studied to reduce the amount of radiation needed for effect RT, including the research presented in this thesis.

Intensity Modulated Radiotherapy limits radiation exposure to healthy tissues because they are prone to secondary carcinomas caused by X-ray exposure.[5] RT is often used in situations where the surrounding tissues could be damaged by surgery; however, in cases like head and neck cancer or testicular cancer, these healthy surrounding tissues are made of up fast-replicating cells which already present a high-risk factor should they become cancerous.

The primary goal of RT is to damage the cells of cancerous tissue such that they are killed or cannot reproduce. Several forms of cellular damage cause cell death or apoptosis, even in cases such as cancer where apoptosis pathways have been affected by mutations. The main method of killing cancer cells in RT is by producing reactive oxygen species (ROS). These are radicals and other highly reactive chemical species include hydroxyl radical, nitrogen dioxide, hydrogen peroxide, and singlet oxygen, all of which can react with lipids and proteins in critical organelles in a phenomenon called oxidative stress. In traditional RT, it is generally accepted that ROS are produced by radiolysis, where electrons are ejected from molecules present in the sample by photons of appropriate energy. Radiolysis may be caused by incident photons, or by secondary photons or excited states that occur as a result of local photon-matter interactions (See Section 1.2). In an aqueous environment, the dominant product of this radiolysis is the hydroxyl radical, followed by dissolved electrons and hydronium radicals.[6] These ROS, being very unstable, do not exist for long before reacting with species in the vicinity of their formation. Whether a low energy photon, low energy electron, or radical is produced, this energetic species can only travel about 10 nm in the cytosolic environment before reacting with another species.[7]

This high reactivity provides a tradeoff, as the same property that makes ROS useful for cell damage necessitates their formation directly next to the target.

1.2. Interactions of X-ray Radiation and Matter
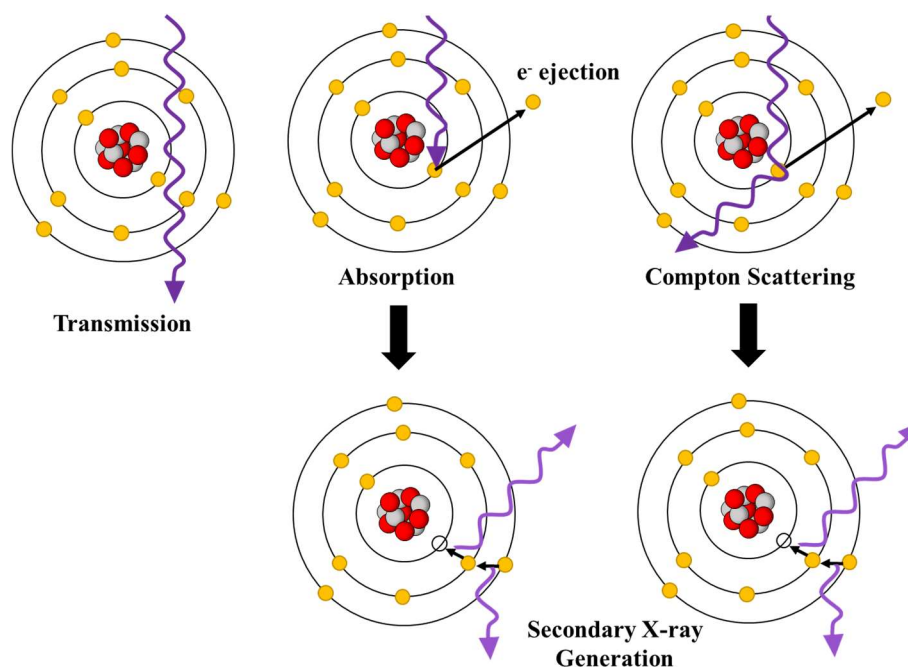
Figure 1.1) Illustrating possible interactions between an atom and an X-ray

The photons that make up X-ray radiation, also referred to as X-rays themselves, have wavelengths between 0.01 to 10 nanometers and energies ranging from 100 eV to 100 keV. While this is the commonly accepted energy range in the field of physics, it is common in the medical field to refer to radiation up to 12 MeV to be referred to as X-rays. Regardless of how they are defined, the interactions of X-rays with matter are dependent on their energy. Further, even a monochromatic X-ray beam can cause various photon-matter interactions to occur, in different proportions depending on the incident energy. Whether using poly- or monochromatic radiation, incident X-rays can be scattered,

absorbed, or transmitted by the atoms of the sample as shown in **Figure 1.1** and described below.

X-ray scattering occurs when an incident photon interacts with matter in such a way that its direction of movement is changed. If the X-ray is simply deflected by an atom in a new direction without energy loss, the elastically scattered radiation is termed Rayleigh scattering. More common, however, is Compton scattering, in which an X-ray interacts with a single electron in an atom. In this inelgalo electron-photon interaction, a fraction of the incident X-ray energy is transferred to the electron before the photon is deflected in a new direction with less energy. The resulting excited electron will in general have enough energy to escape the nuclear attraction of the atom, leaving an ionized atom. The probability of Compton scattering occurring increases with increasing density of the material, and decreases with increasing incident photon energy. Due to the high energy of X-ray photons used in RT, materials with high densities are desirable to increase scattering in specific locations.

When the energy of the incident X-ray is greater than or equal to the binding energy of an electron, quantized X-ray absorption of the incident photon can occur. The energy absorbed by the atom results in the ejection of the electron from its orbital and removes it from the nuclear attraction of the atom. This phenomenon is known as the photoelectric effect. When the X-ray and electron binding energies are similar in magnitude, absorption is highly probable and leads to a spike in the attenuation of X-rays at and above this energy. In any event that an inner shell electron is ejected from an atom, whether it be by absorption or Compton scattering, the empty shell will be filled by an outer-shell electron. The loss of

energy from the outer shell electron upon transition to the lower energy orbital is released as a photon of the same energy as the difference between the orbitals. which can be an ultraviolet photon or an X-ray, referred to as a secondary X-ray. These high energy secondary photons can then go on to excite other molecular and atomic transitions themselves. Depending on the magnitude of the initial excited state and the matter it passes through, this effect can multiply the number of excited states and amplify the number of chemical reactions caused by the single incident photon.

Lastly, and most simply, if an incident X-ray does not interact with any matter while passing through a material, it will be transmitted through the other side without being changed in direction or energy. Diagnostic X-ray imaging relies on transmitted X-rays to strike scintillator materials, allowing for spatial imaging that differentiates between dense, strongly X-ray-interactive tissues like bone and sparse, highly X-ray transmissive regions, like soft tissues or void space.

1.3. Nanoparticles to Enhance Radiotherapy

To address the limitations of RT a field of RT-enhancing NPs is emerging. Through a variety of strategies, these NPs are designed to increase the number of ROS produced upon irradiation of a tissue, as compared to the same radiation dose alone.

1.3.1. Physical Enhancement

$H_2O \rightarrow OH\cdot + e^- + H^+$

$H_2O \rightarrow OH\cdot + e^- + H^+$

$H_2O \rightarrow OH\cdot + e^- + H^+$

4) Any X-rays which escape the NP volume can produce radicals

1) Incident X-ray Enters NP Volume

2) Compton scattering creates secondary X-rays

3) Tertiary, quaternary X-rays may be formed
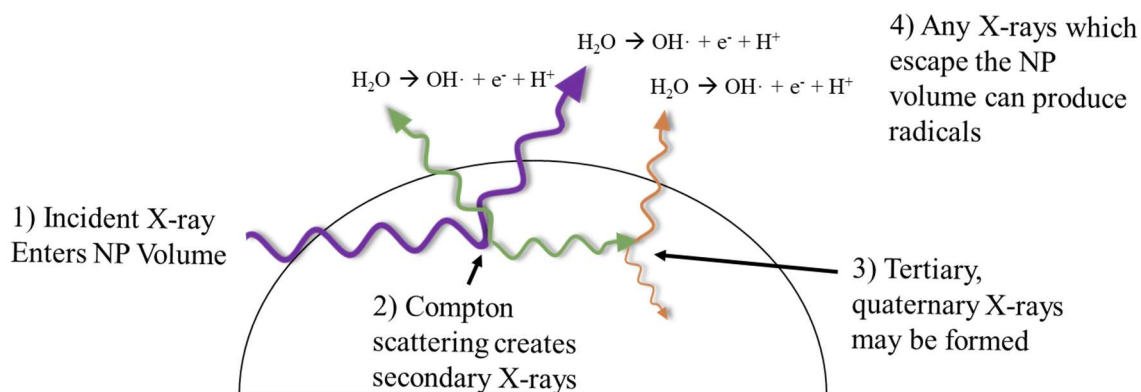
Figure 1.2) One possible interaction of an NP and X-ray enabling physical enhancement of RT.

One method for enhancing RT relies on introducing materials to the cancer tissue that will localize the energy deposition to that tissue, also known as physical enhancement. Inorganic NPs in particular can be applied this way due to their generally high densities and average atomic numbers, as both of these properties allow them to attenuate a much greater number of X-rays than the less dense, lower atomic number materials found in tissues. These dense NPs are intended to scatter and absorb the incident photons such that lower energy photons are produced.[8] These lower-energy photons are more likely to deposit their energy within the tumor volume due to their greater attenuation by the soft tissues. The ideal material for this application would be NPs made of heavy metals due to their high densities, although these come with challenges. Lead is well known to be highly toxic. Tungsten and Iridium are inert in physiological conditions, but the syntheses of their NPs typically produce very small NPs below 10 nm, which are not ideal as they can be filtered out of the bloodstream.[9–11] Gold has historically been the most popular NP material

for this application due to the ease with which NPs can be made, as well as its inertness. However, these biologically inert materials have a flaw in their lack of excretion from the body, leaving this foreign material in the body permanently.[12] This research focuses on the use of bismuth NPs for attenuation(physical)-derived enhancement, made possible with novel synthetic methods for bismuth NPs, bismuth's high density, and its slow but complete oxidation at physiological pH.

1.3.2. Enhancement via Excited States in Nanoparticles, Chemical Enhancement

1) Incident X-ray Enters NP Volume

2) Compton scattering creates secondary X-rays

3) Lower energy excited states in the crystal excite a dopant, generating a photon upon relaxation

4) A photosensitizer on the surface of the NP absorbs the photon and generates a ROS

$^3O_2$

$^1O_2$
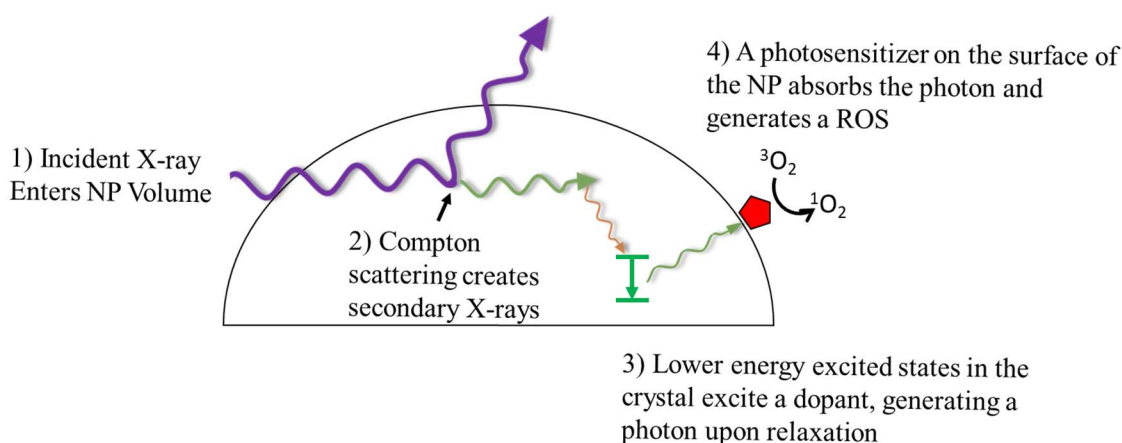
Figure 1.3) Interactions of an NP and X-ray which enable chemical enhancement. Alternate energy pathways are omitted for clarity.

When a material is struck by an X-ray, it can absorb energy and initiate a cascade of secondary transitions. In the case of semiconductor or insulator materials, the lower-energy photons produced can excite the bandgap transition, causing the generation of an electron-hole pair called an exciton. These point charges move around the material until one of two quenching events occur. If they reach the surface, they are trapped by surface defects and react with molecules near the surface. If a positive and negative charge

recombine while in the crystal, the exciton's energy can be converted to a photon which can escape the crystal. This recombination becomes more likely when the crystal contains energy states with an allowed transition between them, meaning that the emitted light can be intentionally tuned to favor a specific wavelength. This can either be accomplished by altering the physical properties of the crystalline matrix, or by adding dopants with accessible energy states. When this process is used to convert X-ray to light in the visible spectrum, the process is called scintillation. Excitons can decay by producing multiple lower energy excitons, until those states escape the NP volume or are thermalized. The energy released upon exciton decay can be emitted from the particle as a combination of photons and chemical bonds at the surface which is unique to the material in question, the volume of the material, as well as the photon energy.

In the enhancement of RT, it is often advantageous to design the NP such that the excitons in the material are directed into a mechanism of producing ROS. This has been executed in titania and silica-based NP systems when irradiated with high energy photons such as X-rays and vacuum UV.[13,14] In fact, silica nanomaterials generate low levels of ROS spontaneously in water, which contributes to the hazard of breathing in silica dust over long periods.[15–17] These mechanisms require reactions between excited states on the NP surface and water, dissolved species in water, or the excited states can cause dissociation of atoms on the surface of the NPs to form ROS.

Another mechanism by which energy can be funneled directly into radical production is the attachment of photosensitizers or other organic molecules to the surface of the NP which can absorb the photons emitted by the NP and excite nearby dissolved

species such as oxygen. Photosensitizers such as Rose Bengal or M450 had been studied previously to absorb energy from an external beam and produce ROS, a process known as photodynamic therapy (PDT). Incorporation of these photosensitizers onto the surface of light-emitting NPs has been studied extensively, as it allows the use of PDT in tissues too deep to reach with an external beam, however, the production of these PDT NPs requires a fine degree of control over the distance between the emitting species and the PS. Energy transfer performed by emission and absorption is inefficient compared to forester resonance energy transfer, which allows the efficient transfer of energy between species with corresponding emissions and absorption within a few nanometers of each other.

1.4. Examples of X-ray Radiotherapy Enhancing Nanoparticles

A variety of NP types have been assessed for their enhancement of cancer cell killing during RT. These types can be separated into two categories, those that enhance damage through their physical properties and those that direct energy to specific radical-producing chemical reactions.

1.4.1. Nanoparticles used in Physical Enhancement

The earliest example of NPs used in RT enhancement was the use of gold NPs by Hainfeld et al. in 2004, in which 2 nm solid gold NPs were injected into mice.[18] The combination of NP administration with RT resulted in the eradication of tumors over a 30 day observation period, while RT alone only delayed tumor growth. The viability of the group treated with NPs and RT was 86%, compared to the 50% treated by radiation alone. The results were impressive, although some shortcomings demanded improvement of the

method. The injected dose into the mice was nearly 25% gold by mass, which leads to issues of viscosity that limit its use as an intravenous agent. The 2 nm diameter of the NPs was also significant, as the NPs had rapid clearance times, with concentrations of gold peaking within 10 minutes of administration and reduced to half after 20-40 minutes, depending on tissue type. These NPs, being very small and unmodified, were rapidly filtered out of the blood by the kidneys and were not able to circulate long enough to accumulate in any intended tissues. The group has continued to research gold NPs for this use until recently, and have recently switched to using iodine-loaded NPs, citing reasons such as "poor clearance" and "cost".[19]

The use of bismuth in the enhancement of RT has also been recorded, with variable compositions and explanations of the dose enhancing effects. Yu et al. synthesized 3 nm Bi NPs by reducing Bi^{3+} salts with oleylamine in the presence of oleic acid, which stabilized the surface as well as acting as a solvent.[20] The resulting hydrophobic NPs were treated with 1,2-diastearoyl-sn-glycero-3-phosphoethanolamine-N-[methoxy(polyethylene glycol)], or DSPE-PEG, which anchored a long PEG strand into the dense alkyl chains on the surface and imparted hydrophilicity onto the NP. In addition to DSPE-PEG, LysP-1 peptides were added as a means of additional targeting to specific receptors on cells. The success of RT enhancement was supported by tumor volume reduction in mice, which showed synergistic effects between Bi NPs and RT. In addition to X-ray irradiation, tumor volumes were also shown to be affected by infrared excitation. As bismuth tends to absorb a large range of radiation wavelengths, this study showed

promise in its application to both deep-seated tumors by X-ray RT enhancement as well as superficial tumors via IR enhancement.

These examples show the potential of heavy metal NPs in the enhancement of RT by improving the energy deposition of X-rays into tumors. To avoid working with these heavy metals, however, other methods have been developed which use various optical matrices to direct the energy to specific radical-producing reactions.

1.4.2. Chemical Enhancement of Radiotherapy using Nanoparticles

Either through directing energy to a radical-producing reaction or by exciting nearby species, specific chemical pathways can be incorporated into the design of an NP to further enhance RT. An NP of the former category is described by Mirjolet et al. who used titanite nanotubes to enhance RT and quantified the enhancement *in vitro*.[13] Titanite nanotubes were synthesized using titanium dioxide powder as a precursor, which was treated in strong basic media within hydrothermal conditions. The resulting nanotubes were several hundred nanometers long, but only 10 nm in diameter, with a 4 nm open channel in the middle. These nanotubes proved non-toxic *in vitro* until X-ray radiation was applied, at which time DNA double strand breaks increased significantly in frequency. The authors credit this increase in DNA damage to the interaction of titanite with water adsorbed on its surface, in which excited states on the surface can hydrolyze water resulting in a similar product to direct water excitation by X-ray.

By far the more popular means of directing energy to radical productions, however, is through the paradigm of Photodynamic Therapy (PDT). Whereas conventional PDT uses

an external beam to excite a photosensitizer, NPs have been developed which use light-emitting NP as a photon source instead, attaching the PS close to the surface. This permits frequency resonance energy transfer between the excited states in the NP and the PS, which is highly efficient. A seminal example of X-ray activated PDT NPs was the use of LaF$_3$:Tb NPs with a variety of porphyrin photosensitizers attached, developed by Tang et al.[21] His group used Tb-doped LaF$_3$ NPs as a photon source and Rose Bengal as a PS, which is well suited to producing singlet oxygen. The design of the NP relied on the LaF$_3$:Tb being porous, which was achieved via a rapid, disordered aggregation of smaller NPs during the synthesis. The pores allowed the PS to be loaded into the volume of the scintillating NP itself, which placed the PS and excited Tb in the crystal very close together. As a result of this closeness, FRET occurred efficiently and 85% of the energy which excited Tb was transferred to Rose Bengal, resulting in a high yield of singlet oxygen.

Another seminal paper in the field of NP-mediated X-ray activated PDT comes from the Chen et al., whose platform included a SrAl$_2$O$_3$:Eu core paired with MC540, a dye which strongly absorbs red light and has been used as a PS to excite dissolved O$_2$ and form singlet oxygen.[22] The PS was housed in a layer of mesoporous silica, which was notably not coated with any biocompatible species. Despite this, the NPs were not toxic on their own and could be completely excreted by mice within 16 days. With radiation applied, however, significant enhancement of radiation damage was observed *in vitro* through cell viability and *in vivo* through tumor volume measurements. Whereas untreated mice or other forms of control mice saw tumor volume increases of 800%, mice cotreated with the NPs and X-ray radiation showed no tumor growth.

1.5. Scope of this Work

Given the interest in using NPs to enhance RT, this thesis involves the synthesis of two NP types with this capability. The primary focus of the work is the synthesis of these NPs and their modification to adapt them to biological environments, with preliminary assays performed to assess their usefulness as RT enhancers.

Chapter 2 describes the synthesis of bismuth nanoparticles. Bismuth is a high-Z, high-density material capable of scattering X-rays far more often than biological tissue, amplifying the effect of an incident photon during RT. A novel synthesis has been developed which negates several of the difficulties of making Bi NPs by providing an aerobic procedure which occurs in only a few hours. Details have been provided on the optimization of this procedure to produce uniform 55 nm NPs. In addition, details regarding the coating of silica onto that surface, and the subsequent attachment of PEG to the silica, provide a route to an NP suitable for biological environments.

Chapter 3 describes the synthesis and characterization of a CaF_2-core mesoporous silica-shell NP, designed as a physical and chemical enhancer of RT. The tunable emissions of CaF_2 NPs may enable photocatalyzed reactions near the NP, or even fluorescence imaging. In this case, they were designed to physically scatter X-rays and amplify the effect of an incident photon during RT, while acting as a radioluminescent material. Detailed characterization of the CaF_2 NPs at different stages and in different synthesis conditions show the development of their structure and X-ray luminescent properties. An optimization of mesoporous silica coating has been presented, allowing for a flexible scaffold for small

molecule loading or surface species attachment. A procedure for PEG attachment has been optimized and applied.

Chapter 4 includes experiments that assess the usefulness of as-prepared NPs as RT enhancers. Fluorescent probes have been used to assess the radical production during irradiation. *In vitro* assays have been performed to assess the biocompatibility of these materials, as well as viability once they are excited with X-ray. A preliminary *in vivo* biodistribution assay has been performed in mice, which supports claims that they can be degraded over a short period.

CHAPTER 2 – A NOVEL SYNTHESIS OF BISMUTH NANOPARTICLES AND

THEIR MODIFICATION WITH SILICA SHELLS

2.1. Introduction

Bismuth nanoparticles (Bi NPs) have many characteristics that make them candidates as physical enhancers of RT. The synthesis of these NPs, however, can be difficult to control. In this introduction, the essential theory of how metallic NPs are synthesized and how this theory relates to Bi NPs will be discussed.

2.1.1. Synthesis of Metallic Nanoparticles

The synthesis of metallic NPs, such as the Bi NPs in this work, can be examined through the lens of classical nucleation theory, the most complete framework of colloid growth available today[23–25]. To describe the theory in general, we will use the widespread paradigm of metal ions being reduced to their zero-valence states and formed into NPs. A metal ion is placed into a controlled redox reaction in which it will be reduced into individual metal atoms. These atoms serve as the monomer, the smallest building block of the NP. This monomer is unstable in solution, but can become more stable by agglomerating with identical monomers. After several dozen monomers aggregate this way, they form a nucleus, a semi-stable solid upon which other monomers can adsorb. Once the nucleus crosses a certain volume threshold for the system, it becomes a NP that will continue to grow until the monomer-producing reaction is complete. However, should the nucleus fail to grow fast enough, it may destabilize and release its composite monomers back into the system.
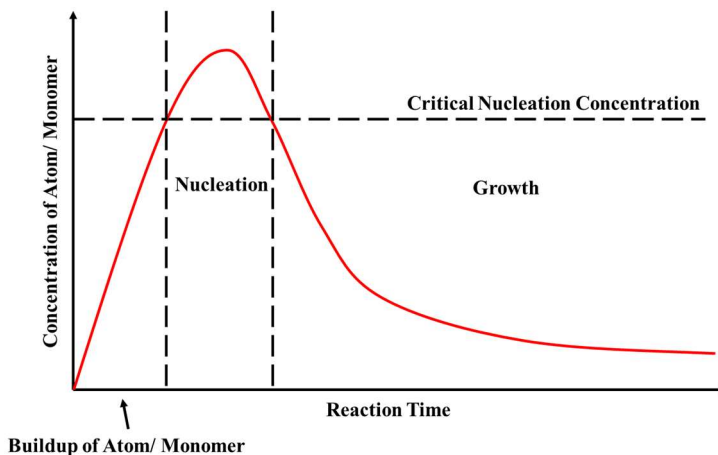
Figure 2.1) Depiction of the different phases of NP formation and the effects of atom monomer concentration.

The key to producing uniform NPs in this type of synthesis is to achieve an event called burst nucleation. **Figure 2.1** graphically describes the ideal stages of NP nucleation and growth throughout a monomer-producing reaction in relation to monomer concentration. The monomer concentration must build in the solution until it reaches the critical nucleation concentration, the concentration at which solid formation is a spontaneous process, driven by the thermodynamic advantage of minimizing the high-energy surface area of the monomers. Then, a large number of nuclei form simultaneously in the nucleation step. They then quickly adsorb most of the monomers in solution, reducing the monomer concentration and preventing further nucleation. Monomer formed later in the reaction or left over after this step can be adsorbed onto the NPs during the final growth phase of the reaction.

Staying above the critical nucleation concentration for a short period is essential, as NPs which nucleate at the same time and grow in the same environment will be uniform

in diameter. Nucleation over an extended period will lead to a variety of growth times, leading to a distribution of NP sizes. On the other hand, if a nucleation period is too short or does not produce enough nuclei, the concentration of monomer in solution may rise above the critical nucleation concentration again and create new nuclei with shorter growth times. An understanding of how different reaction parameters affect the production and sequestration of monomer can guide decisions in the design of a synthesis to cause a single significant nucleation event to occur.

There are a variety of parameters that can be altered to optimize the nucleation step in a NP synthesis. Altering a single parameter will rarely have a single effect, however, we can categorize these modifications into those that modify the reaction rate of monomer production and those that control the formation of solids. In the case of a metal ion reduction reaction, the amount of reducing agent present is the most direct way to alter the monomer production rate, along with the concentration of the metal ion. The temperature of the reaction is important for many syntheses of this type, as well as the presence of any catalysts. These variables alter the length of time that the system will spend above the critical nucleation concentration, but that nucleation concentration can be altered by the presence of surface stabilizers. By anchoring themselves onto the nuclei surfaces, they can negate much of the surface area's high energy states. The solvent system's ability to stabilize individual atoms also affects the rate at which those atoms are forced together into nuclei. Finally, the NP growth period must occur when most of the monomer has been already sequestered into nuclei and monomer production is slower than earlier in the

reaction. The growth stage can be detrimental if the rate at which monomers are produced is too fast and another nucleation event occurs.

2.1.1.1. Syntheses of Bismuth Nanoparticles

Syntheses of Bi NPs can be separated into two categories, the polyol method, and burst nucleation. In the polyol method, a polar bismuth complex is dissolved in a liquid polymer with oxidizable functional groups (e.g., PVP, PEG). When the complex is heated to reaction temperatures (140 – 200 ºC), Bi^{3+} is reduced through the oxidation of the polymer. Despite being used to make metallic NPs for over 25 years, the mechanism by which the metal is reduced is largely unexplored.[26] Nonetheless, the polyol method has distinct advantages over organic-phase methods. The greatest advantage is that the as-prepared Bi NPs are water-dispersible without the need for further ligand exchanges, making the product of these syntheses useful for aqueous applications. However, the greatest drawback of the polyol synthesis is the limited control over mean Bi NP diameter. In the most cited published polyol synthesis, uniform Bi NPs were produced by reacting a Bi^{3+}-acetate complex with PVP.[27] This reaction generated size and shape uniform Bi NPs ranging from 115 to 600 nm depending on reaction parameters. Unfortunately, this synthesis was limited to producing uniform Bi NPs with sizes greater than 115 nm and was not applicable to the synthesis of smaller Bi NPs.

The best-described methods in the production of uniform Bi NPs enable the burst nucleation of NPs in non-coordinating solvents. A common feature of these syntheses is the addition of a powerful reducing agent to produce a "burst" of nucleated NPs which quickly deplete the available bismuth in solution. High boiling, non-coordinating solvents,

such as alkylbenzenes and higher alkanes, are suitable solvents for burst nucleation syntheses while amines and thiols are the most popular complexing and reducing agents. These conditions improve the reproducibility of NP nucleation by standardizing nucleation temperatures and bismuth complex concentrations at the time of reducing agent addition. While there is sufficient literature precedence for the success in controllably synthesizing uniform Bi NPs, these syntheses are limited by their use of organic bases and air-free techniques which increase the difficulty and exclusivity of their use.[28–30] These methods have been thought necessary due to the relative ease of the oxidation of Bi^{3+}, and indeed bismuth precursors used in burst nucleation synthesis are only stable in air or light for a matter of minutes.[31] As a result, these precursors must be prepared in glovebox environments and ideally stored in refrigerated, light-free, air-free conditions.[32] Also, bismuth compounds typically have poor solubility in nonpolar solvents, which is addressed by complexation of bismuth with reductive thiols, amines, or phosphines with long, branched alkyl chains. The use of phosphines requires that the reactions be done in an anaerobic atmosphere, and so their use is less practical in terms of reaction scaling in comparison to amines or thiols. When organic bases are applied to rapidly reduce a bismuth precursor, the issue of precursor storage is circumvented. However, in the synthesis reported by Kovalenko et al., the authors are upfront about the extensive safety considerations taken in their synthesis.[28] The procedure involves the injection of n-BuLi into a 160 °C bismuth precursor solution. The reaction requires strict air-free conditions and extensive drying steps before this injection to ensure the safety of the base addition.

Despite these disadvantages, the advantages of Bi NP synthesis in non-coordinating solvents have allowed for several syntheses of highly uniform NPs over a range of sizes. The use of non-coordinating media affords greater control over the concentration of complexing ligands which can bind to bismuth and exchange it between NPs in the growth phase. In a polar coordinating solvent, solvent molecules can behave as carriers which can rearrange the bismuth between NPs, leading to Oswald ripening. Oswald ripening occurs when monomers exchange between slightly smaller, less stable NPs and slightly larger, more stable NPs. The smaller NPs lose bismuth faster than they adsorb it, making them smaller, with the opposite happening on the larger NPs. The result of this Oswald ripening is the divergence of previously uniform NPs into distinct smaller and larger populations. In non-coordinating solvents, these carriers are limited to the ligands which originally solubilized and reduced the bismuth.

The most facile, reproducible uniform Bi NP synthesis to date was published by the Buhro group in 2008 and functions as the starting point for the work described in Chapter 2.[29] In this synthesis, bismuth-bis(trimethylsilyl)amide is dissolved in diisopropyl benzene (DIPB), along with PVP-graft-hexadecene as a surface stabilizing polymer and excess sodium bis(trimethylsilyl)amine, all under a nitrogen atmosphere. Upon heating the system to 180 °C, NPs nucleate. After 18 hours of stirring at reaction temperature, the products of the reaction are monodisperse spherical Bi NPs of sizes between 3 and 115 nm, depending only on the amount of sodium bis(trimethylsilyl)amine present in solution. While this synthesis offers excellent size control and monodisperse products, the preparation of bismuth-bis(trimethylsilyl)amine is rigorous, requiring strict air-free techniques and n-

BuLi, followed by careful storage and use to address the precursor's high air and light sensitivity.

2.1.2. Motivation and Scope for this Work

Bi NPs are potential physical enhancers of RT due to their high density, atomic number, and biodegradability. The synthesis of Bi NPs can be complicated by the air and light sensitivity of bismuth species used as precursors, traditionally necessitating air-free techniques. In this work, an aerobic synthesis is presented which requires no specialized equipment or techniques, enabling the synthesis of this useful product. After developing the synthesis of the Bi NPs, a silica shell addition procedure was developed to allow the covalent attachment of surface species which could further facilitate the Bi NP's use as an intravenous agent.

This chapter describes an aerobic synthesis of Bi NPs with average diameters in the range 40-80 nm using commercially available bismuth triiodide as starting material; the method uses only readily available chemicals and conventional laboratory equipment. Furthermore, NP diameter data from replicates of the synthesis indicate that this method is highly reproducible in achieving Bi NP populations with low standard deviations in the mean diameters. The reaction results from the reduction of a soluble alkylammonium iodobismuthate precursor species formed immediately before NP formation. At some concentrations of iodobismuthate anion, burst nucleation of Bi NPs results from the reduction of Bi^{3+} by the coordinated iodide ligands when a threshold temperature is exceeded. Finally, phase transfer and silica shell addition of the Bi NPs are described, which results in stable aqueous colloids with retention of size, morphology, and colloidal

stability. The resultant, high atomic number, hydrophilic Bi NPs prepared using this synthesis method have the potential for application in X-ray RT enhancement.

2.2. Experimental

2.2.1. Materials

The following chemicals were purchased and used without purification: For Bi NP synthesis, parameter variations, and controls: BiI_3 (99.999%, Strem), $BiBr_3$ (98%+, Sigma-Aldrich), $BiCl_3$ (98%+, Acros), KOH (99%, VWR), di-isopropylbenzene (98%, 2:1 mixture of m and p isomers, Acros), 1-hexadecylamine (90%, Technical Grade, Alfa Aesar), poly(1-vinylpyrrolidone)-graft-(1-triacontene) (PVPT) (Sigma-Aldrich), hexane (ACS grade, mixture of isomers, Fisher), and ethanol (ACS grade, Fisher). For phase exchange: chloroform (ACS grade, Fisher), and poly(1-vinylpyrrolidone) 29k MW (Sigma-Aldrich). For silica shell: tetraethoxysilane (98%, Sigma-Aldrich), and ammonium hydroxide (30% aq. solution, Fisher). In the water control reaction, phase exchange, and silica shell procedure, electrophoretically pure H_2O (18 MΩ•cm resistivity) was used. All reactions, purifications, and analyses were performed in ambient laboratory air and light conditions unless otherwise indicated.

2.2.2. Bismuth Nanoparticle Synthesis

Standard safety precaution: All procedural steps were carried out in a chemical fume hood; caution must be taken due to the release of I_2 gas.

In a typical synthesis, 300 mg BiI_3 (0.51 mmol, 1 equiv) was loaded into a 100 mL one-neck round bottom flask and dispersed in 16 mL of di-isopropylbenzene (DIPB),

producing a solution with a BiI_3 concentration of 0.32 M. This suspension, containing colorless solvent and black BiI_3 as a dispersed solid powder, was stirred at 650 rpm and heated to 180 °C for 15 minutes. At 180 °C, I_2 was observed to evolve as a purple gas. A solution color change (to pale orange) was also observed, in addition to the formation of a brown-orange solid suspended in the mixture. The temperature was subsequently lowered to 100 °C, followed by the addition of 3.75 g of hexadecylamine (HDA) (15.5 mmol, concentration 95.0 M, 30.4 equiv) and 345 mg poly(1-vinylpyrrolidone)-graft-(1-triacontene) (PVPT). This suspension was then stirred open to the atmosphere for 30 minutes, resulting in an opaque orange suspension. The flask was then stoppered and stirred at 100 °C for an additional 30 minutes, during which time, no additional changes to the atmosphere in the flask were made. The temperature was then raised to 180 °C over a period of 2.5 minutes. During heating, the orange solution color gradually intensified, and within seconds of reaching 180 °C, became a homogeneous black colloid. The reaction was allowed to proceed at 180 °C for 12.5 minutes before it was quenched (total reaction duration including heating interval = 15 minutes). To quench the reaction, the flask was removed from heat and cooled in a room temperature water bath for one minute. To isolate the Bi NPs, a 50 mL mixture of 1:1 hexane: ethanol was added to the reaction flask, followed by collecting the contents in a conical tube, sonicating for one minute, and centrifuging at 3000 rcf for 15 minutes. The Bi NPs were twice re-dispersed and centrifuged out of solution using 80 mL of 1:1 hexane: ethanol. The Bi NPs could then be stored, either as a stable colloid in toluene or as a fully re-dispersible (in toluene) dry

powder. After drying, the mass of the NPs was approximately 82 mg (82.1 ± 5.5 mg, n=5), which represents a 77% yield if the NPs are assumed to be entirely bismuth by mass.

2.2.3. Organic to Aqueous Phase Transfer

To achieve phase transfer of the PVPT-coated Bi NPs to water, it was necessary to further coat the as-prepared NPs with hydrophilic, unmodified poly(1-vinylpyrrolidone) (PVP). To accomplish this, ~100 mg of Bi NPs (a typical yield when using the standard reaction conditions) were dispersed in 50 mL of chloroform by sonication, followed by the addition of one gram of PVP (29k MW) to the flask. The solution was subsequently stirred at reflux for ~10 hours. The Bi NPs were then collected by centrifugation. Excess PVP was removed by twice re-dispersing the Bi NPs in 25 mL of ethanol followed by centrifugation. The solid obtained by centrifugation was then dried in air at 125 °C for 15 minutes.

2.2.4. Silica Shell Addition

As-prepared PVP-coated Bi NPs (~20 mg) were dispersed in a solution containing 90 mL ethanol and 10 mL deionized H_2O by sonicating the mixture for ~30 minutes. Subsequently, 2 mL of 30% aqueous ammonium hydroxide (NH_4OH) and then 25 μL of tetraethoxysilane (TEOS) (0.11 mmol, 0.011 mM) was added while stirring. Stirring was continued for 30 minutes at room temperature, and then the flask was moved to a 4 °C freezer and cooled for ~15 hours. Silica-coated Bi NPs were collected by centrifugation. The silica-coated Bi NPs were isolated by twice re-dispersing them in 25 mL of ethanol followed by centrifugation, then dried at 80 °C.

2.2.5. Crystallographic, microscopic, and spectroscopic characterizations of Bi NPs

Bi NP imaging was performed on a Technai F20 TEM operating at 4500 eV and equipped with an Oxford Instruments EDX detector. Samples were prepared by drop casting Bi NP dispersions in toluene (~4 mg/mL) onto type-B carbon-coated copper TEM grids (Ted Pella product #1844-F). Samples were allowed to air-dry for at least 10 minutes at room temperature followed by at least 5 minutes at 125 °C. Images were processed using the FIJI software package. All mean diameter and standard deviation data were derived from at least 200 NP diameter measurements per synthesis. For any TEM image used, all NPs in the image were included to eliminate selective measuring.

X-ray diffraction samples (XRD) were prepared by drying Bi NPs or other solid precipitates in a drying oven at 125 °C, then grinding them into a fine powder using a mortar and pestle. These powders were then placed in a zero-background (Si (100)) micro-holder slide. Characterization was performed using a Rigaku Ultima IV X-ray diffraction system in focused beam (Bragg-Brentano) geometry with graphite monochromatized Cu K_α radiation.

FT-IR spectra were obtained using a Thermo Scientific Nicolet iS10 spectrometer fitted with an attenuated total reflectance attachment having a diamond window. Solid samples were first heated at 125 °C to volatilize solvents, then placed directly on the diamond window and compressed.

2.3. Synthesis of Bismuth Nanoparticles from an Iodobismuthate Precursor and Investigation of Reaction Mechanism

2.3.1. Products of the Standard Bi NP Synthesis
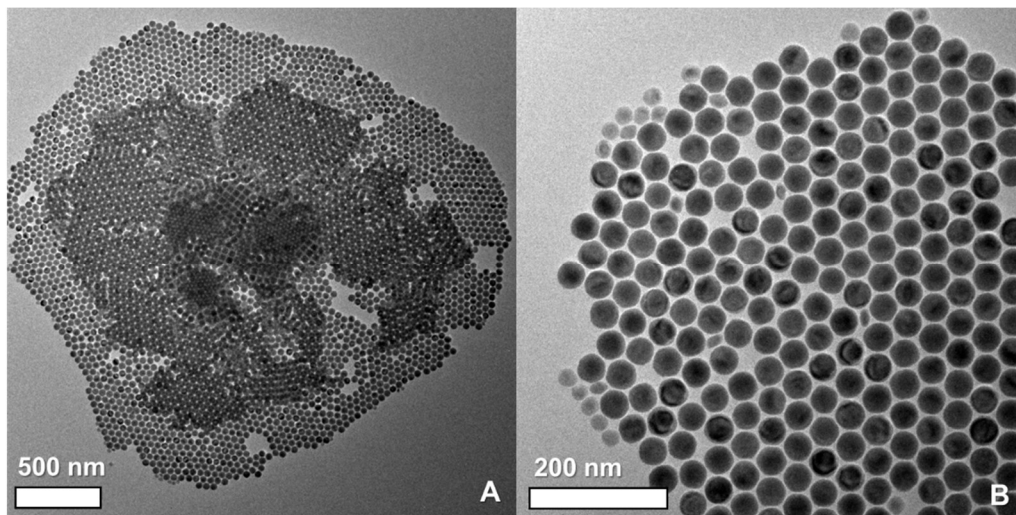
Figure 2.2) TEM images of bismuth nanoparticles produced from standardized reagent amounts. Images A and B were taken at different sites within the same TEM sample.

This synthesis with "standard" reagent amounts presented in section 2.2.2 produces highly monodisperse Bi NPs which are, on average, 65 nm in diameter (**Figure 2.2A**). Some batches feature smaller, 10 nm NPs along with the predominant larger populations (**Figure 2.2B**). These smaller populations make up small fractions of the product mass and have negligible effects on the properties of the resulting batch. Interestingly, these smaller species appear to take on slightly flattened hexagonal shapes which indicate a very slow growth rate, implying that they were formed later in the reaction when most of the bismuth had already been reduced. An examination of 5 consequent batches produced by identical procedures showed a deviation of 16.3% from the pooled average size of 58.1 ± 9.5 nm, however, there were no significant outliers present in any batch that would disqualify the products from being useful as intravenous agents.

Table 2.1) NP diameter data collected from 5 subsequent batches of as-prepared Bi NPs, collected by analysis of TEM images

Sample Number	Mean Diameter (nm)	Standard Deviation (nm)	% Std. Dev.
1	37.0	5.9	15.9
2	60.3	9.8	16.3
3	49.7	4.1	8.2
4	75.9	10.0	13.2
5	67.4	8.7	12.9
Pooled (1-5)	58.1	9.5	16.3

2.3.2. Instrumental Analysis of Bismuth Nanoparticles

XRD analysis of the as-prepared NPs showed the expected pattern for metallic bismuth. Peaks were observed at 2θ positions which can be indexed to the expected planes of metallic bismuth (**Figure 2.3**). The line broadening observed in the XRD pattern can be used in conjunction with the Scherrer equation (Equation 1)

$$\tau = \frac{K\lambda}{\beta cos\theta}$$

Equation 1) The Scherrer equation, used in X-ray crystallography to determine crystallite size.

to measure the average crystallite size of the NPs (t is mean crystallite size, K is the shape factor which is assumed as a sphere, λ is the X-ray wavelength, and θ is the X-ray angle). The average crystallite size calculated from the Scherrer equation using the pattern of sample 5 from Table 2.1 was 68.2 nm, which corresponded to measurements taken from TEM images which were analyzed by measuring individual NPs, resulting in a mean size of 67.4 ± 8.7 nm. This is important because it indicates that the NPs are single crystals. Whereas similar preparations of metallic NPs can involve the aggregation of smaller crystalline domains to make larger particles, that can be ruled out in this case.[23] Alternatively, these single crystals can be explained as a crystal grown from a single unit cell, although this is unlikely as the NPs are not shaped like the orthorhombic cell of metallic bismuth. Instead, the Bi NPs are most often spherical, probably because the rate at which bismuth is added to their surfaces is too fast to be affected by the energetic differences between adding to specific facets. Oriented growth was observed, however, in two instances: Oswald ripened particles after 20 hours and small NPs amongst populations with larger diameters. In these instances, the addition rate of bismuth to the NP surfaces may have been slower than during the main growth phase of their syntheses, allowing facet adsorption differences to take greater effect.
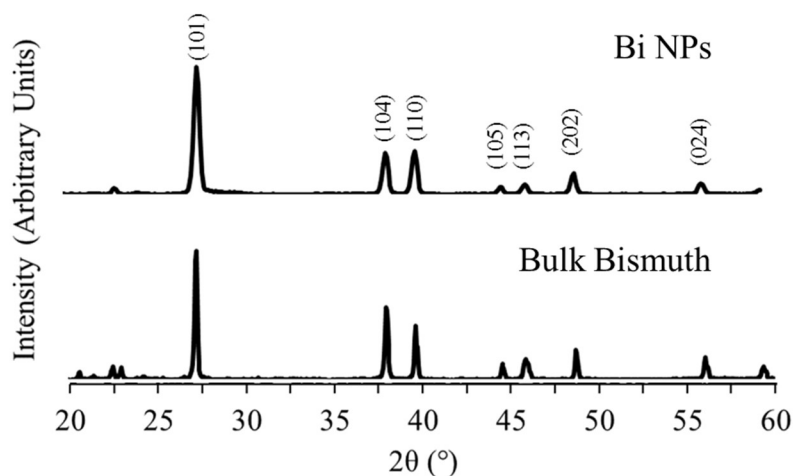
Figure 2.3) Powder XRD patterns of as-prepared Bi NPs and bulk metallic bismuth

2.3.3. Reaction Mechanism Controls
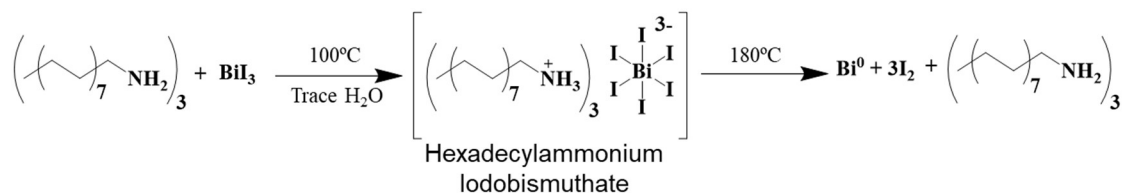
Scheme 2.1) Reaction used to produce metallic bismuth

Several factors motivated the use of an iodobismuthate precursor. It is relatively facile to form due to the principles of hard-soft acid-base theory, in which both Bi^{3+} and iodide are highly polarizable ions that can bind strongly to each other. The Bi^{3+} cation is then near six iodide anions with high oxidation potentials. It was hypothesized at the outset of this study that the iodide could act as a reducing agent for the Bi^{3+} (Scheme 2.1). The iodobismuthate which results carries a negative charge, which can be stabilized by a variety of compounds that are typically present in NP syntheses that bind to charged surfaces and expose long hydrophobic moieties to the organic solvent. In this case, it is most likely an

alkylammonium iodobismuthate produced by the protonation of HDA. This proposed mechanism was supported by replacing bismuth iodide with either bismuth chloride or bismuth bromide in equimolar amounts, which led to no bismuth reduction in the case of the chloride and a lower yield of metallic bismuth in the case of the bromide. This observed trend aligned with the strengths of these halides as reducing agents, in which iodide has the highest oxidation potential of these three.[33] The NPs produced from the bromide reaction took on a mix of spherical and cubic morphologies (**Figure 2.4**); controlling this anisotropy was not further investigated. Anisotropic growth can occur due to the influence of surface stabilizers or slow growth rates. As the surface stabilizer concentration was unchanged from the standard synthesis conditions, it is more likely that this anisotropy resulted from the slower production of Bi^0 when bismuth bromide was used as a precursor.
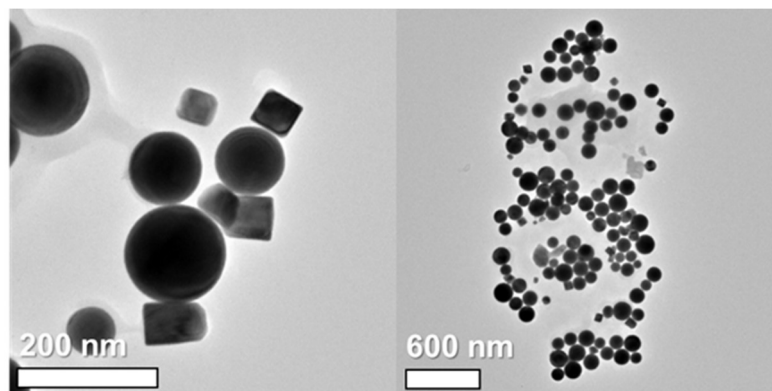
Figure 2.4) Bi NPs produced using BiBr$_3$ as a bismuth source.

In the first heating step of the reaction, before the HDA is added to stabilize iodobismuthate, an orange solid is formed as the bismuth iodide is heated to 180 °C. This solid was isolated and examined with XRD (**Figure 2.5**), and the pattern matches that of bismuth oxyiodide (JCPDS card number 10-0445). While it is undetermined if this impacts the monodispersity of the resultant NPs, it is most likely that the removal of some I_2 from the reaction modifies the rate of the bismuth reduction reaction to make a single nucleation event more likely.
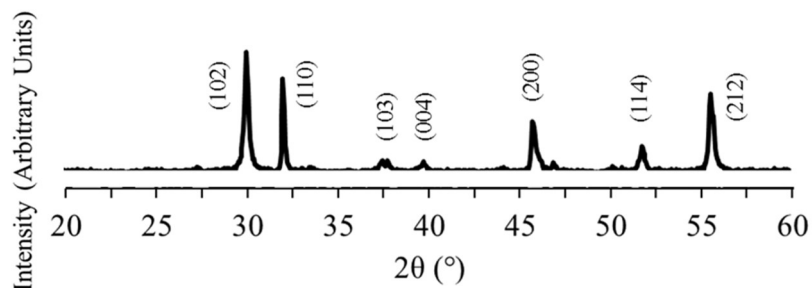
Figure 2.5) XRD pattern of bismuth oxyiodide produced during the first heating step of the Bi NP synthesis

2.3.4. Survey of Parameters for NP Nucleation and Growth

After the 65 nm NP synthesis was established, modifications to that procedure were performed with two goals: to establish the mechanistic roles of the reagents in the synthesis and attain different sizes of NPs from a similar procedure. The latter motivation would provide options for NP diameters in later efforts to optimize the biodistribution of the NPs in the bloodstream. Parameters altered in this study were the amounts of HDA, bismuth iodide, polyvinylpyrrolidone-graft-triacontene (PVPT), as well as reaction time. This

survey of parameters yielded a variety of correlations when analyzed via classical nucleation theory, as described in this chapter's introduction.
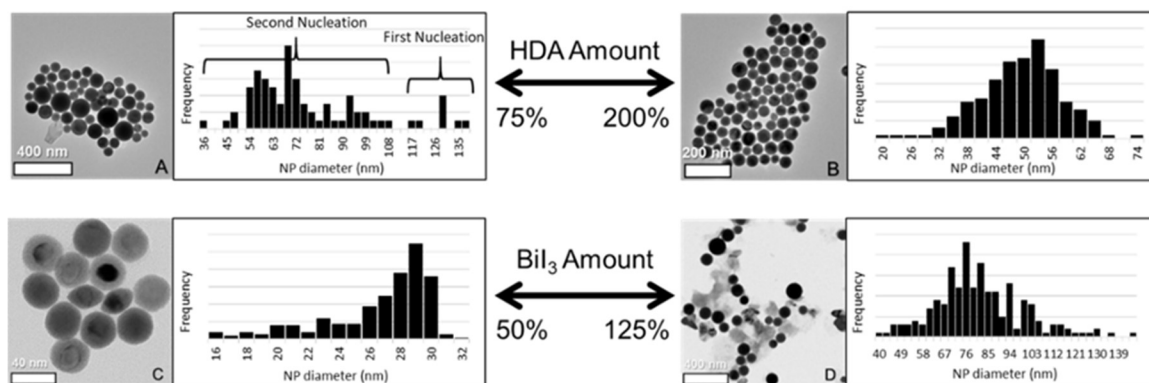
Figure 2.6) Size histograms and TEM images illustrating the effect of changing HDA and BiI₃ concentrations on resultant NP diameter distributions

It was hypothesized that increasing the amounts of the two main components of the iodobismuthate, bismuth iodide and HDA, would produce broadened NP diameter distributions. A higher concentration of iodobismuthate at the time of reaction should increase the rate of Bi^0 production and cause an extended nucleation period, leading to many different growth times and a spectrum of NP diameters. In contrast, reducing the amount of these two reactants was hypothesized to result in multiple distinct diameters of NPs (i.e. a mix of 20 nm NPs and 50 nm NPs), as a slower rate of bismuth reduction would lead to fewer nuclei being formed, leaving them unable to completely adsorb the bismuth in solution, resulting in multiple minor nucleation periods. To assess these hypotheses, the amount of HDA and BiI₃ added to the reaction were altered, with "100%" of these amounts fixed at the concentrations presented as the standards in section 2.2.2.

Increasing the BiI_3 by 25% resulted in a range of diameters between 40 and 120 nm while doubling the amount of HDA provided a range between 30 and 70 nm (**Figure 2.6**). These broad NP diameter distributions can be interpreted to mean that the nucleation periods in these reactions were extended. Reducing the amount of HDA to 75% of the standard value resulted in two distinct size populations at 50-80 nm and 130 nm, which could have been the result of two well-defined nucleation events. Interestingly, the reduced amount of bismuth iodide led to single populations of smaller NPs with ~30 nm diameters in some trials, however, in repeated trials this result could not be consistently reproduced. One interpretation of this result is that a similar number of nuclei formed as in the standard synthesis, but grew for shorter periods due to the lesser availability of bismuth.

50% PVPT
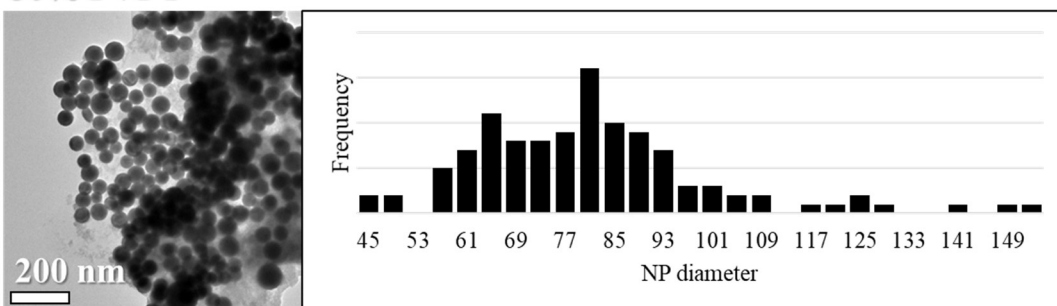
200% PVPT
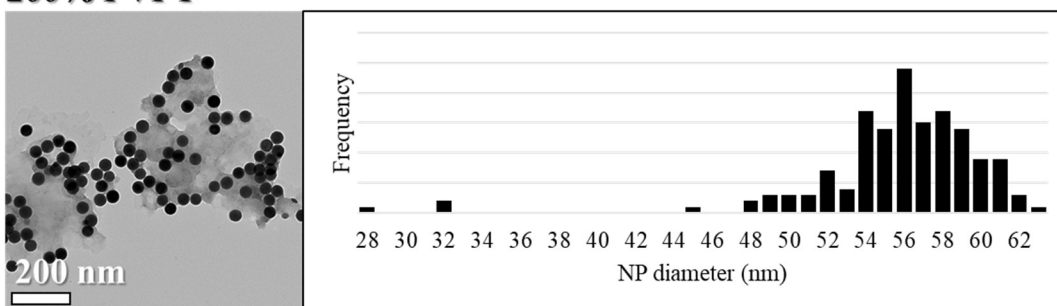
Figure 2.7) TEM images and NP diameter histograms from the analysis of Bi NPs with (Top) 50% or (Bottom) 200% of the standard concentration of PVPT.

According to classical nucleation theory, a higher amount of surface stabilizer should better stabilize nuclei as they appear in the nucleation stage, resulting in a greater number of smaller NPs after the growth stage is complete. As such, it was hypothesized that increasing the amount of PVPT in the reaction would result in smaller NPs and decreasing the amount of PVPT would result in larger NPs. While the minimum tested PVPT concentration (50% of standard) was found to produce larger NPs, these larger sizes were dispersed between 60-90 nm, with a mean diameter and standard deviation of 84±20 nm. The lesser amount of PVPT appeared to have affected the synthesis as hypothesized, producing a larger mean diameter, but at the cost of the uniformity of the population. The maximum amount of PVPT tested was 200% of the normal value, which produced a

population with 55±4 nm diameters, which was uniformly sized and within the range of sizes expected of the standard synthesis (**Figure 2.7**). The greater amount of PVPT did not significantly shrink the diameter of the population, and further increasing the PVPT amounts prevented the isolation of the NPs well enough for TEM analysis. While the hypothesized result was not observed, the insensitivity of the synthesis to higher PVPT concentrations appeared positive for the synthesis' robustness.
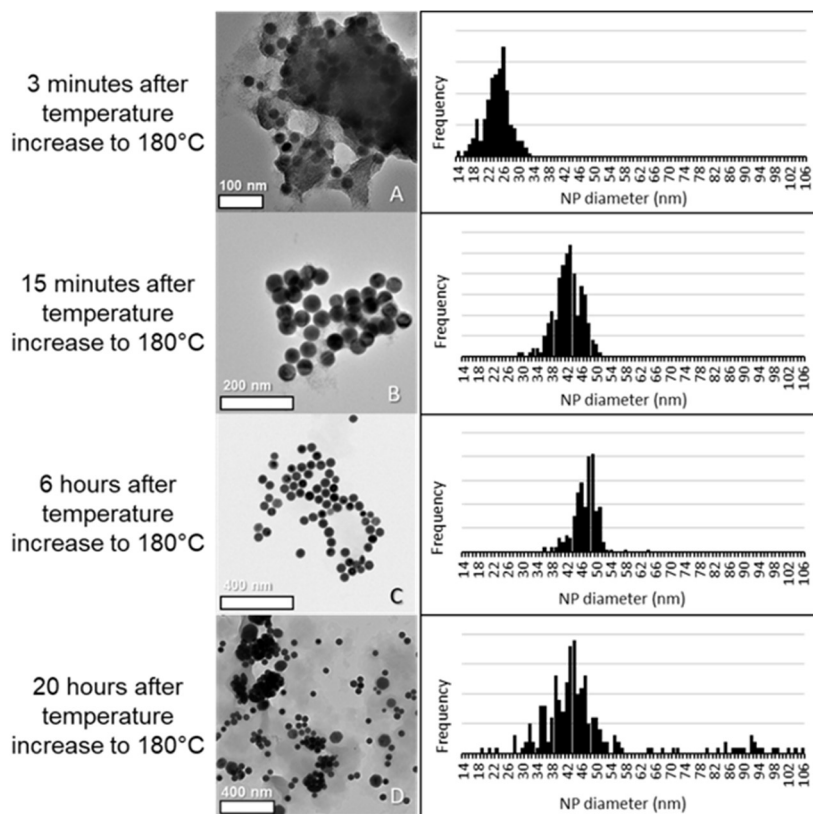
Figure 2.8) TEM and size distribution histograms of the standard Bi NP synthesis stopped at different time points.

Stopping the reaction at different time points provided insight into the growth patterns of these particles. The bismuth collected in the Bi NPs after the standard 15 minute reaction time consistently provided yields above 90%, suggesting that the bismuth reduction was complete after this point. It was hypothesized that shorter timeframes would result in uniform, but smaller NPs as the nucleation step would be identical but the growth time would be reduced. Longer reaction times were hypothesized to induce Oswald ripening, producing populations with NP diameters which diverged after a period of uniformity. Nucleation was observed and marked as the moment the solution could be deemed optically "black", which consistently occurred less than 2 minutes after the hotplate reached 180 °C. Whereas the reaction was normally quenched 15 minutes after this point, timepoints were also taken 3 minutes, 6 hours, and 18 hours afterward (**Figure 2.8**). Results from the 3-minute timepoint showed uniform small particles with 25 ± 3.3 nm diameters as well as a greater amount of leftover organic material than results from the standard synthesis. Due to the size of the NPs, their similarities in solubility and dispersibility to leftover organic species, and the low yield associated with stopping the reaction before full bismuth reduction, this shorter reaction period was not used as a source of smaller Bi NPs. The NPs recovered at each subsequent time point had larger diameters, with NP growth complete at a time point between 10 minutes and 6 hours. In the period between 6 hours and 18 hours, Oswald ripening began to take place at an accelerated rate. Interestingly, the larger NPs that form from this process appear to take on flattened, hexagonal shapes. The NPs are crystals with orthorhombic unit cells, and given a very slow addition of bismuth to the surfaces of these crystals, growth along some planes will be

faster than others, leading to the observed shapes. One practical conclusion that came from these experiments was that Oswald ripening required a much longer heating time than the standard reaction period, and is not a likely source of deviation in sizes in the previous experiments. This result supported the design of the synthesis in a non-coordinating solvent system, as Oswald ripening occurs much quicker in coordinating solvents.

2.4. Silica Shell Addition

2.4.1. Bi NP Nonpolar-to-Polar Phase Transfer

After a procedure for reproducible monodisperse Bi NPs was developed, a silica shell was added such that silanes and biologically active molecules could be attached. Many reactions are available for generating silica nanoscale structures; however, these are typically performed in polar media and the presence of water. The as-synthesized Bi NPs were coated in hydrophobic triacontene moieties, preventing their dispersal in polar solvents. A procedure was needed to render the Bi NPs hydrophilic while maintaining the NPs' uniform morphologies.
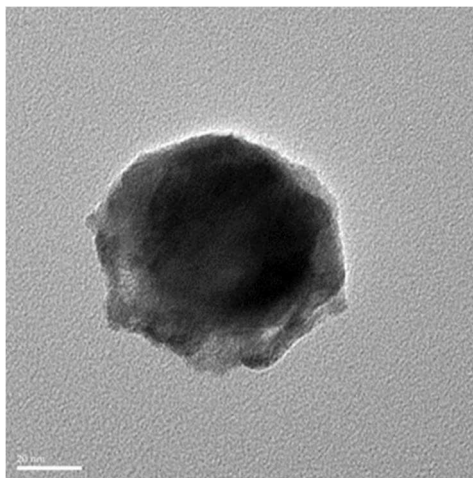
Figure 2.9) Bi NP degraded by a phase transfer process performed in a biphasic hexane/water mixture.

The first attempts at this phase transfer involved biphasic systems in which hydrophobic Bi NPs were dispersed in a layer of hexane above an aqueous layer saturated with ligands which would, hypothetically, bind to their surfaces. Whether attempted with thiols or polydentate binding ligands like citrate, and regardless of sonication, stirring, or other methods of layer mixing, the bismuth oxidized upon contact with the aqueous layer. This can be inferred from TEM images of Bi NPs treated with aqueous citrate, which shows that their smooth, spherical morphologies have been damaged and left with rough surfaces (**Figure 2.9**). In response to this, future attempts were performed in non-oxidizing aliphatic solvents which could disperse the NPs individually as well as to solubilize the incoming polar ligands. Phase exchange was finally achieved by dispersing the PVPT-coated Bi NPs in chloroform with a large excess of polar, unmodified, long-chain PVP. After heating for several hours, the resulting NPs had excellent hydrophilicity and were not oxidatively degraded when analyzed by TEM. However, it could not be supported that the PVPT had

been removed and replaced. Marked differences in the IR spectrum of Bi NPs before and after this treatment indicate that change has occurred, but the similarities between the PVPT and PVP make it impractical to determine a ratio of the two polymers on the surface of the NPs. IR spectroscopy of the as-prepared NPs shows peaks at 2916 cm^{-1}, indicative of the C-H bonds seen on the triacontane moiety of the PVPT. sp2 C-O bonding is observed as well at 1653 cm^{-1}, provided by the PVP backbone of the PVPT (**Figure 2.10**).
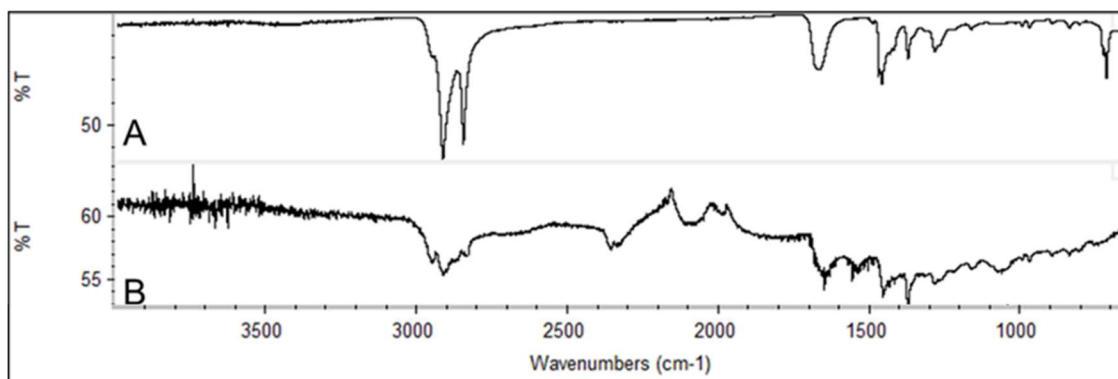
Figure 2.10) Infrared transmission spectra of A) Bi NPs after synthesis and B) Bi NPs after phase exchange treatment with PVP

2.4.2. Silica Shell Addition Experiments

With the Bi NPs rendered hydrophilic, the silica could then be layered onto the surface of the NP. This procedure follows a common structure in which tetraethoxysilane (TEOS) was hydrolyzed in basic conditions, substituting ethoxy groups for hydroxyl anions. This forms orthosilicic acid, which can then polycondense in a dehydration reaction to form silica. The silanol groups on the surface of the silica granules are partially deprotonated at basic pH, giving the surface a negative surface charge, and they adsorb

onto   the   positively   charged   Bi   NP   surface   (Scheme   2.2).
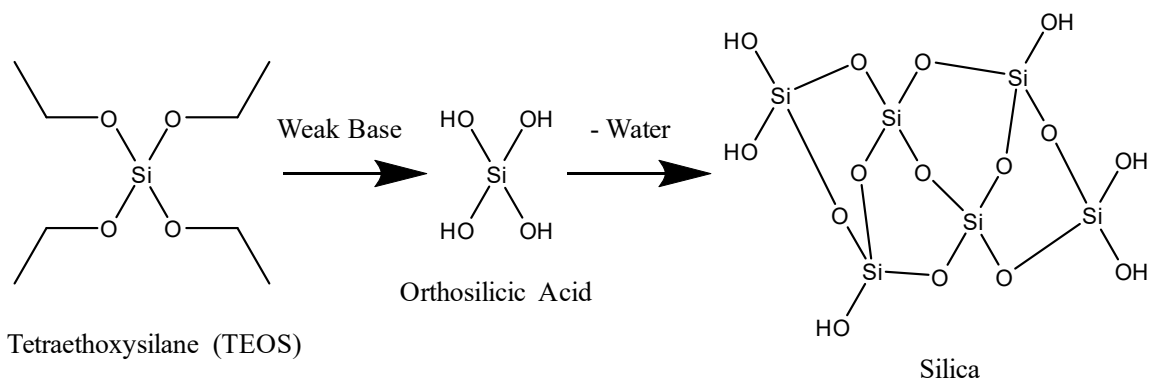
Scheme 2.2: Generalized Formation of Silica from Tetraethoxysilane
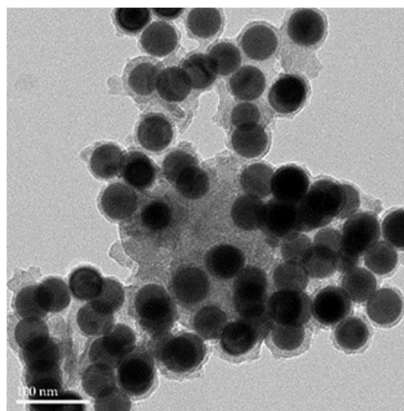
Figure 2.11) Silica shells on Bi NPs before optimization.

This synthesis structure had to be modified, however, due to issues which arose when the products were produced when stirring at room temperature overnight. These particles tended to aggregate together into large clusters, as well as take on ragged, sharp shells (**Figure 2.11**). These ragged shells were attributed to the rapid production of orthosilicic acid at room temperature. In these cases, large grains of silica were able to

condense and attach to the Bi NPs, leading to the rough surface texture. To slow down this reaction and form finer silica material, the reaction was briefly stirred with the TEOS at room temperature and proceeding with the reaction for 12 hours at 4 °C with no stirring. This solved both issues of ragged surfaces and clusters of particles, leading to NPs with smooth, individual shells (**Figure 2.12A**). The composition of the shell was supported by EDX and IR spectroscopic analysis, the former of which shows that the shell layer is comprised of silicon and oxygen, and the former spectrum containing a predominant peak at 1045 cm^{-1} which can be correlated to Si-O bond stretching (**Figure 2.12B, C**).
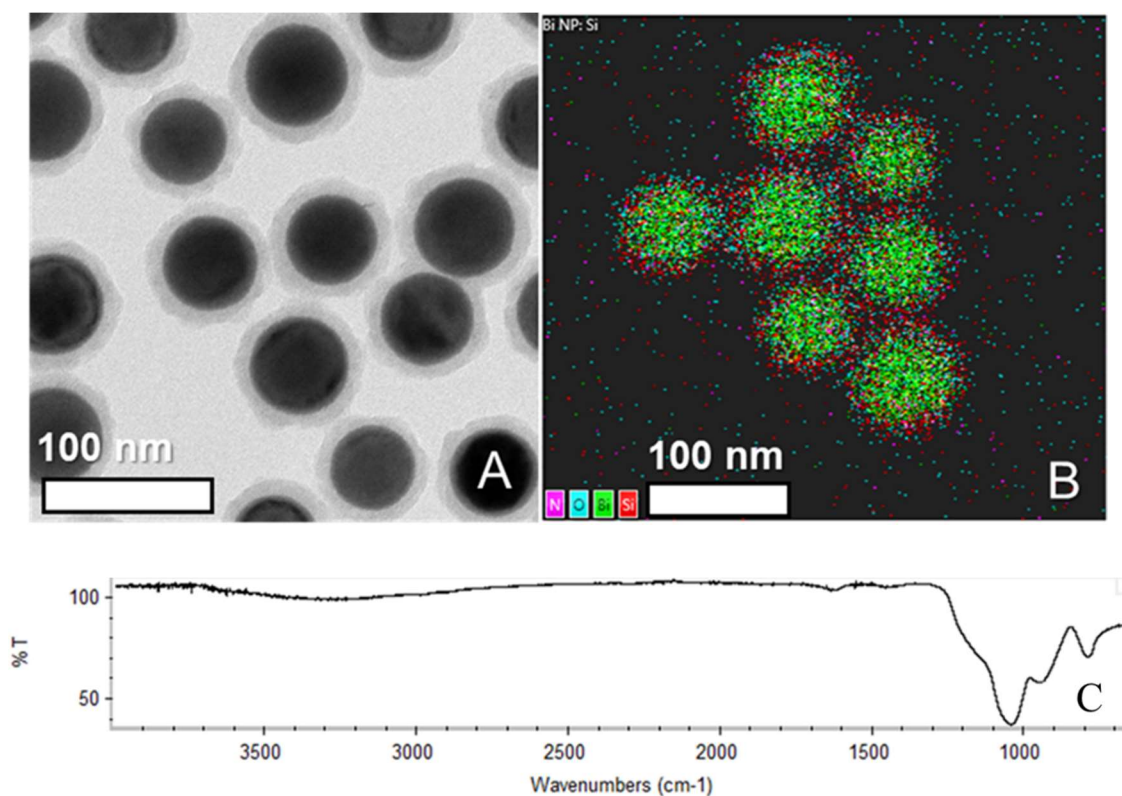
Figure 2.12) (A) Silica shell on Bi NPs after optimization. (B) EDX mapping performed on Bi NPs with silica shells. (C) Infrared transmission spectrum of Bi/Silica NPs.

The thickness of the silica shell was optimized by adding variable amounts of TEOS to the reaction. An ideal silica shell would be as thin as possible to minimize the additional NP diameter necessary for this reactive scaffold. A minimal concentration of 25 μL TEOS per 200 mL reaction volume was found to completely coat the NPs in thin 10 nm silica shells. Lesser amounts led to the presence of uncoated NPs. A modicum of control over the silica shell thickness could be attained in the TEOS amount range from 25 to 100 μL, with 100 μL of TEOS producing a 25-30 nm thick silica shell. However, when the amount of TEOS was increased to 500 and 1000 μL, empty silica objects began to appear, with most of the mass in the 1000 μL trial being silica only (**Figure 2.13**). These empty silica objects are formed when the silicic acid concentration in solution reaches its critical nucleation concentration, and the clustering of this monomer leads to the formation of silica nuclei. In reactions without empty silica, the silicic acid and silica concentrations stayed low enough to avoid the creation of nuclei, while adding monomers onto the already-existing solids.
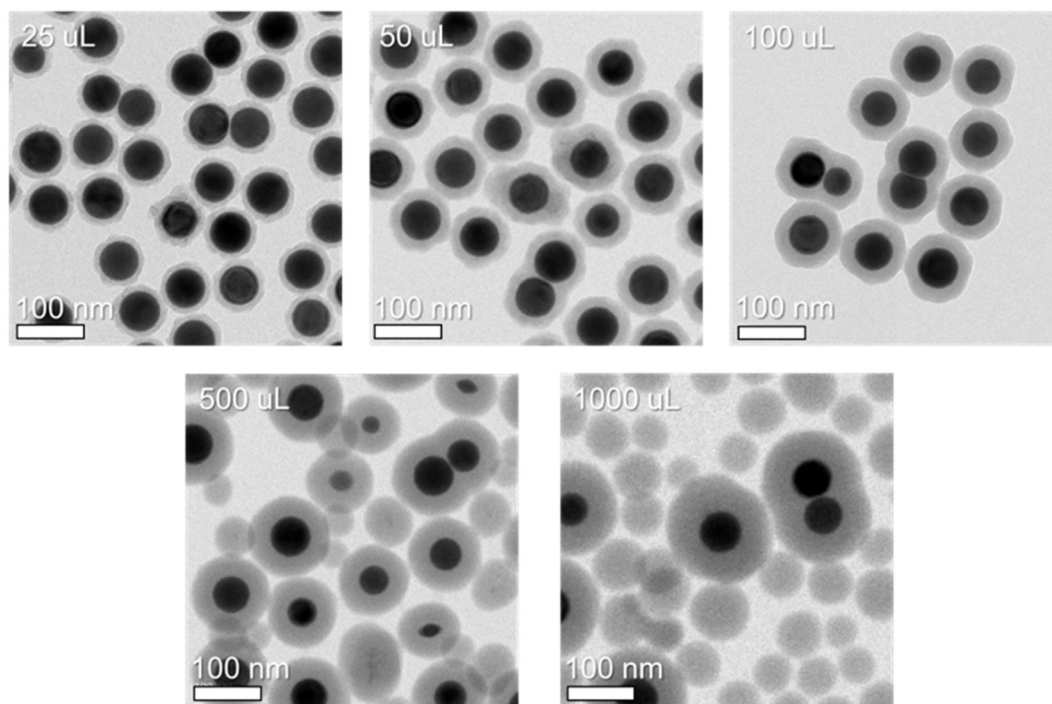
Figure 2.13) Bi NPs coated in Silica as a result of varying concentrations of tetraethoxysilane in solution.

As this silica layer was only intended to serve as a scaffold, efforts were made to produce thinner shells. These efforts were not successful. Further reducing the concentration of TEOS in solution produced uneven, patchy shells and stopping the reaction at various time points was not successful due to residual silicic acid in solution. Upon stopping the reaction, ethanol is removed via rotary evaporation and then the remaining aqueous solution is centrifuged. During these processes, small silica objects are produced which cannot be easily removed due to their similar properties to the coated Bi NPs.

2.5. Conclusions

In this chapter, the synthesis of Bi NPs and their modification with silica shells were described. The synthesis of uniform Bi NPs has been performed in literature, however, these syntheses rely on reagents and techniques that are hazardous and sensitive to air and light. This synthesis is an aerobic one-pot synthesis that forms an iodobismuthate precursor immediately before reducing the bismuth to nucleate NPs. The mechanism of this reduction has been explored by substituting the iodide for bromine or chloride, resulting in little or no Bi^0 formation due to their lesser reducing abilities. Parameters that affect the growth of the NPs have also been investigated, including the amount of surface stabilizer, stabilizing alkylamine species, and reaction time. While many of these factors affected the system in ways predicted by classical nucleation theory, the complexity of the system sometimes did not produce such results. Lastly, after the NPs were synthesized, they were coated in a 10 nm-thick layer of silica which served as a reactive attachment site for silane species and rendered the NPs hydrophilic. Several experiments involving reaction time, temperature, and the amount of silane precursor were performed to achieve a reproducible shell addition. This modification left the NPs fit for further assessment as RT enhancers, which was further probed in experiments discussed in Chapter 4.

CHAPTER 3 - SYNTHESIS AND CHEMICAL CHARACTERIZATION OF

MESOPOROUS SILICA-COATED CALCIUM FLUORIDE NANOPARTICLES

3.1. Introduction

3.1.1. Synthesis of Ionic Crystal Nanoparticles

NP syntheses most often strive to attain uniform NP products of a certain target size and crystallinity. When the product is an ionic nanocrystal that is insoluble in water, there are complications that must be surmounted to attain these goals. These ions that are strongly attracted to one another tend to react quickly when combined, resulting in uncontrolled precipitation. In terms of classical nucleation and growth theory, rapid monomer production and NP nucleation make it difficult to control nanocrystal size. Without *in situ* control over the reaction speed, it becomes important to control the speed at which the nanocrystal component ions are introduced into the system. This can be done simply with a dropwise addition or using a precursor technique where the nanocrystal's component ions are produced from other soluble reactants (such as organometallic precursors).

Rapid precipitation is also expected to result in relatively more nanocrystal defects relative to slow precipitation under thermodynamic control. Under kinetic control, once the ions are in solution, they will rapidly associate with each other, too rapidly to allow a highly ordered lattice to form. In many applications of nanocrystals, it becomes important to improve the quality of the lattice, which can improve desirable properties such as density, spectral absorptivity, or photoluminescence intensity. To do this, one can heat

anneal the primary nanocrystals after they are formed, which generally results in decreased defect sites due to greater mobility of the lattice ions at higher temperatures. In the process of doing this, however, smaller crystallites can be fused together to form larger species in a process that is very difficult to control, so that large size variations in the diameters of annealed NPs may result. If bringing the nanocrystals up to high temperatures undesirably sinters them (*e.g.,* into a polycrystalline solid), or if drying them would result in worse aggregation, then a hydrothermal cell may become a better option. These Teflon-lined heavy steel vessels can be used to crystallize ionic nanomaterials in aqueous solution at moderate temperatures (~200 ºC) by a process known as hydrothermal annealing, which is assisted by the high pressure that builds within the closed system. To avoid aggregation during hydrothermal annealing, components such as organic surface stabilizers (surfactants) can be used at these temperatures and pressures, which provides a means of controlling nanocrystal growth while improving crystallinity (since organic surfactants are known to be somewhat kinetically labile in terminating the surface of ionic nanocrystals).

The incorporation of dopants into ionic crystals without change of structure type is most easily accomplished by choosing dopant ions of the same oxidation state and similar ionic radius to the ion on the lattice site that one would like to dope. The incorporation of a dopant ion with a different oxidation state can be compensated for by inclusion of additional dopants into the crystal to balance charge (e.g., an interstitial proton to balance an excess negative charge), or by means of lattice vacancies. These are viewed as defect sites within otherwise periodic nanocrystals, and dopants and defects can have significant impacts on the nanocrystal physical, chemical, and photochemical properties. In more

complex cases, it is more likely that the crystal will change to an entirely different phase to accommodate the dopant.

3.1.1.1. Synthesis of Calcium Fluoride Nanoparticles

Calcium fluoride is a popular optical matrix in the study of luminescent materials. CaF_2 crystallizes into a face-centered cubic structure. The high symmetry of the cation sites as well as the similarity in ionic radius between Ca^{2+} and various fluorescent lanthanide ions make the inclusion of such dopants straightforward and permits the symmetries of their excited states. The large bandgap of CaF_2, 12 eV, along with a low phonon energy limits the loss of energy to non-radiative decay and limits radiative decay besides the excitation of dopants. Due to these properties, a variety of syntheses have been developed to make doped CaF_2 NPs for photonics-based applications, including those in the biomedical field. Syntheses of CaF_2 NPs are most often performed using coprecipitation procedures in either water or short-chain alcohols.[34–37] The high affinity of Ca^{2+} for F^- makes coprecipitation an accessible, but difficult to control process, as the reaction occurs very quickly. Hydrothermal annealing is often employed after coprecipitation to improve the crystallinity of the rapidly formed precipitate.

As an RT-enhancing material, the use of CaF_2 is rare. To date, only one other study has been published on the design of a CaF_2 NP for X-ray activated therapy. In that work, Zahedifar *et al.* studied the use of RL-active CaF_2:Tm NPs to excite Protoporphyrin IX (a porphine-based photosensitizer) during X-ray irradiation.[38] The results of this study showed good overlap between the RL emission of the NPs with the absorption band of the photosensitizer, and indirect measurements of singlet oxygen generation suggest that the

platform could be useful in ROS generation enhancement.[38] Moving forward, this NP system could prove promising for RT as it is designed to absorb and localize energy from X-rays which may also increase the localized production of ROS. The work in this thesis involving CaF_2:Ln NPs goes beyond this work by adding a mesoporous silica shell to the NP, allowing for covalent bonding to the surface not possible in the cited study, as well as ROS production and *in vitro* assays which investigate the types and quantity of ROS produced during irradiation.
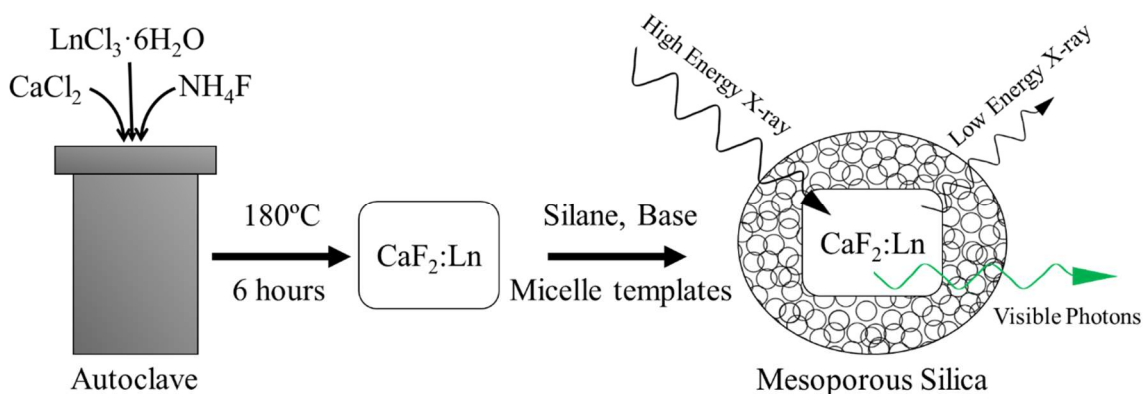
Figure 3.1) Graphic abstract of the synthetic steps described in this chapter

3.1.2. Scope of this Chapter

In this work, CaF_2:Ln NPs have been synthesized, surface coated appropriately for biomedical usage, and studied as RT-enhancing NPs under laboratory-simulated radiotherapeutic conditions. This method capitalizes on the ease of synthesis of coprecipitation methods and the larger single-crystal NP diameter accessed through hydrothermal annealing. The resulting single-crystal NPs are radioluminescent (RL), enhanced by their increased crystal size which lessens the escape of excited states to surface

defects. With this functioning RL agent enabling multimodal imaging, the NPs' surface required modification to enable their use in biological conditions. The surface of ionic crystal NPs such as this tends to be difficult to covalently attach surface species to, however, this limitation was surmounted using a layer of mesoporous silica (MS) modified with PEG for the sake of biocompatibility. Various conditions for applying MS and PEG to the surface were tested, and conditions were found that produced thin, reproducible MS layers and dense layers of PEG. With these syntheses established, this dense inorganic NP with RL capabilities was prepared for RT enhancement experiments.

3.2. Materials and Methods

Materials: The following chemicals were purchased and used without purification: For CaF_2 synthesis: $CaCl_2$ (99%, anhydrous, Acros), $TbCl_3 \cdot 6H_2O$ (99%, Acros), $EuCl_3 \cdot 6H_2O$ (99%, Sigma Aldrich), Sodium citrate dihydrate (99%, J.T. Baker), Ammonium fluoride (98%, Sigma-Aldrich), ethanol (95%, Fisher). For Mesoporous silica coating: Cetyltrimethyl ammonium bromide (99%, Research Organics), ethanol (200 proof, Decon Labs), tetraethoxysilane (98%, Sigma-Aldrich), triethylamine (99%, Acros), 2-[methoxy(polyethyleneoxy)9-12propyl]trimethoxysilane (tech grade, 70+%, Gelest). For ROS quantification assays: aminophenyl fluorescein (APF, 99%, Thermo-fisher), Singlet Oxygen Sensor Green (SOSG, 99%, Thermo-fisher). (All reagents in all experiments used as received)

3.2.1. CaF$_2$ and Ln-doped CaF$_2$ nanoparticle syntheses

In a typical synthesis, a 50 mL round bottom flask was loaded with calcium chloride, or calcium and lanthanide chlorides (Tb^{3+} or Eu^{3+}). The reagent masses used are detailed in Table 3.1 and were chosen to target nanomaterials with ~20 atomic percent Ln dopant in place of Ca ions.

Table 3.1) Metal chloride masses added to flasks to attain certain doping amounts

Synthesis Target (Dopants in Atomic %)	Calcium Chloride Mass (mg)	Doping Metal Chloride Mass (mg)
Undoped CaF$_2$ NPs	388	None
CaF$_2$:Tb 18% NPs	350	93 TbCl$_3$·6H$_2$O
CaF$_2$:Eu 18% NPs	350	90 EuCl$_3$·6H$_2$O

The resulting concentrations in solution were then 126.14 mM CaCl$_2$ and 9.96 mM LnCl$_3$·6H$_2$O. For undoped CaF$_2$ NPs, the CaCl$_2$ concentration was 139.84 mM (3.5 mmol, 1 equiv). Along with the metal chlorides, 5.17 g (0.7 M, 5.0 equiv) of sodium citrate dihydrate was added, followed by 22 mL of distilled water. This solution was stirred for 10 minutes to allow the solids to dissolve completely. Meanwhile, 322 mg (8.7 mmol, 1.74 M, 2.49 equiv) of ammonium fluoride was dissolved in 5 mL of distilled water in a 15 mL centrifuge tube. This solution was loaded into a burette. Then, while still under continuous stirring, ammonium fluoride solution was added dropwise into the round bottom flask containing the metal chloride solution, at a rate of approximately one drop per second.

After all the fluoride solution was added, the slightly turbid solution in the round bottom flask was divided evenly into three 20 mL Teflon autoclave liners, which were placed in stainless steel autoclaves (Parr) and rapidly heated to a temperature of 180 °C for 6 hours. Following heating, the autoclaves were subsequently cooled to room temperature, and the product solutions in the three autoclaves were collected together into a 50 mL centrifuge tube. Then, 10 mL of ethanol (95%) was added, and the product suspensions were centrifuged to isolate the NPs. The NPs were again redispersed, in a solution of 5 mL of water and 35 mL of ethanol, followed by centrifugation. This process was repeated until the dark carbonized species left over from the reaction were no longer present. Finally, the CaF_2 (or CaF_2:Ln) NPs were dried overnight at 50 °C, then crushed to a fine powder using a mortar and pestle and stored for further use.

3.2.2. Mesoporous Silica Coating

Into a 250 mL round bottom flask were added 54 mg of dried, powdered CaF_2 NPs and 100 mL of distilled water, followed by sonication for 30 minutes. Then, 10 mL of ethanol (200 proof), 84 µL of triethylamine (6.02 µmol, 5.48 µM), and 1.8 g (4.94 mmol, 44.9 mM of cetyltrimethyl ammonium bromide (CTAB) were added to the flask. The reaction mixture was next heated to 80 °C and stirred at 1400 rpm with a 3 cm almond-shaped stir bar, which resulted in the formation of CTAB micelles. Next, 300 µL of tetraethoxysilane (TEOS) was added to the flask dropwise over 20 seconds. The flask was subsequently heated and stirred for an additional 30 minutes to accomplish the hydrolysis and polycondensation of the TEOS around the CTAB, followed by cooling in a stirring water bath for 60 seconds. The reaction products were then collected in centrifuge tubes,

followed by centrifugation to isolate the silica-coated CaF_2 NP products. The silica-coated CaF_2 NPs were next resuspended in 20 mL of ethanol (200 proof), followed by 10 minutes of sonication. This colloidal suspension was subsequently transferred to a 100 mL round bottom flask, and then 2 mL of concentrated hydrochloric acid was added to remove the CTAB within the silica network and render the silica coating mesoporous (MS = mesoporous SiO_2). The resulting colloidal solution containing the MS-CaF_2 NPs was stirred and heated to 80 °C for 30 minutes. Then it was cooled in a stirring water bath, and solids were collected by centrifugation. The isolated MS-CaF_2 NPs were purified two cycles of redispersion in a 1 mL water and 20 mL ethanol solution, followed by centrifugation. Finally, the MS-CaF_2 NPs were dried at 50 °C, milled to a powder in a mortar and pestle, and stored for further use.

3.2.3. Surface modification by covalent attachment of polyethylene glycol

15 mg of MS-CaF_2 NPs were suspended in 20 mL of distilled water in a 100 mL round bottom flask, followed by sonication. While stirring at room temperature, 40 μL of ammonium hydroxide (30% w/w in water) was added, followed by 100 μL of 2-[methoxy(polyethyleneoxy)9-12propyl]trimethoxysilane (PEG-silane). After PEG-silane addition, the reaction mixture was left stirring at room temperature for two hours. At the end of this time, the reaction products were poured into a centrifuge tube, and 10 mL of ethanol was added to flocculate the pegylated MS-CaF_2 NPs (PEG-MS-CaF_2 NPs). The PEG-MS-CaF_2 NPs were collected by centrifugation, followed by resuspension in 10 mL of 1:1 water: ethanol and centrifuging, and additional purification by 2 more cycles of redispersion and centrifuging with 10 mL of ethanol. Finally, the PEG-MS-CaF_2 NP

products were dried overnight at 50 °C, then crushed to a fine powder using a mortar and pestle, and stored for further use.

3.2.4. Instrumental Analysis

The NP products through the stages of synthesis were characterized using a combination of transmission electron microscopy (TEM), energy dispersive X-ray spectroscopy (EDX), X-ray diffraction (XRD), radioluminescent spectroscopy, and x-ray photoelectric spectroscopy (XPS).

Transmission Electron Microscopy was performed on a Tecnai F20 TEM operating at 4200 eV. Samples were prepared by dispersing NPs in ethanol (ACS) at concentrations of approximately 1 mg/mL and drop-casting a single drop onto type-B carbon-coated copper TEM grids (Ted Pella Product #1844-F). These samples were dried at room temperature for 10 minutes before drying in a 50 °C oven for at least one hour before imaging. The mean diameters of the NP samples were determined by analyzing several TEM images, corresponding to different (representative) areas of each sample grid. ImageJ software was used to measure the NPs and produce size distributions; each reported size value is based on the minimum requirement to measure at least 200 NPs. To prevent measurement bias, the minimum criteria for an individual image used in mean diameter determination were that it must include at least 50 NPs and that all NPs in the image had to be measured. EDX measurements were taken using the same instrument in scanning-TEM mode and collected using an Oxford Instruments EDX detector.

X-ray diffraction patterns were collected using a Rigaku Ultima IV X-ray diffraction system using graphite monochromatized Cu Kα radiation. Samples were prepared by grinding dry powders in a mortar and pestle and placing them in a glass sample holder. Patterns were collected at a rate of 1 degree per minute from 20 to 60° 2θ. The resulting data was analyzed using Rigaku PDXL2 software. FT-IR spectra were obtained using a Thermo Scientific Nicolet iS10 spectrometer fitted with an attenuated total reflectance attachment having a diamond window. Solid samples were first dried of solvents by heating at 125 °C, then placed directly on the diamond window and compressed.

For the Ln-doped, CaF_2 NPs, photoluminescence (PL) spectroscopy was performed using a Shimadzu RF-5301PC fluorimeter. The Ln-doped, CaF_2 NPs colloidal solutions used in these measurements were prepared by sonicating the corresponding dry powders in water at a concentration of 1 mg/mL. X-ray excited luminescence spectra were also acquired, using 30 mg of dry Ln-doped CaF_2 NP powder for each measurement, and a CellRad Faxitron X-ray system operating at 130 kV and 5 mA as the excitation source; no beam filter was applied. The X-ray excited luminescence was recorded using a StellarNet Silver Nova 200 spectrometer attached to a collimating lens via armored fiber-optic cable (Thorlabs). These measurements were collected with an integration time of 30 seconds.

X-ray Photoelectron Spectroscopy (XPS) was performed on a Versaprobe II XPS/AES featuring an aluminum X-ray source. Samples were prepared for XPS measurements by drop-casting NP suspensions in methanol onto individual aluminum foil substrates heated at 50 °C, followed by drying the samples under vacuum at room

temperature for 12 hours before placement in the XPS transfer arm. Once in the vacuum

chamber, the samples were bombarded with X-rays from the source, in circular spots with

diameters of 100 um. The electron beam used in these experiments was operating at 125 V

and 50 W, and charge balancing was provided by both an e-neutralizer and argon-derived

ion beam. The spectra were calibrated to the carbon 1s peak present in each spectrum

3.3. Synthesis of CaF₂ NPs and Impacts of Hydrothermal Annealing on Crystallite Size
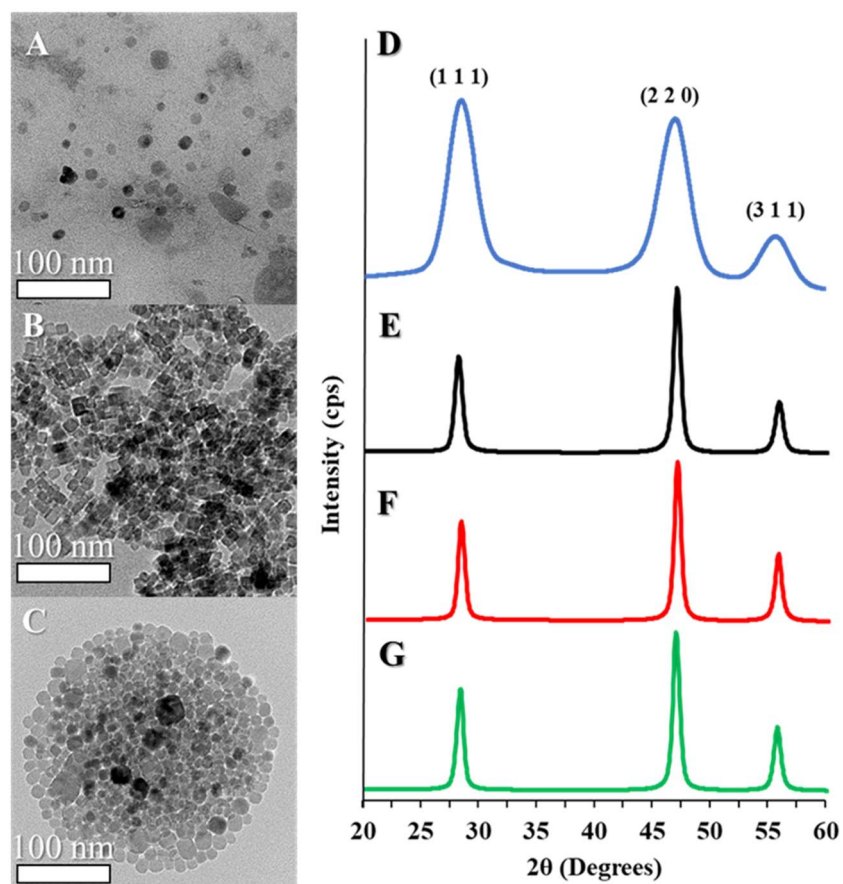
Figure 3.2) TEM images of (A) CaF₂ NPs before and (B) after hydrothermal annealing, and (C) Tb-doped CaF₂ NPs after hydrothermal annealing. XRD patterns of CaF₂ NPs (D) before and (E) after hydrothermal annealing, and (F) Eu-doped and (G) Tb-doped CaF₂ NPs.

Synthesis of CaF₂ NPs was achieved by a modified method adapted from Pedroni et al., who developed a synthesis to study near-IR to visible photon conversion in NP optical matrices.[39] In this procedure, an aqueous solution containing calcium ions, or

calcium and lanthanide ions, is introduced to a separate solution of fluoride ions within an environment highly concentrated with citrate. The citrate acts as a steric and electrostatic surface stabilizer. Due to the large lattice enthalpy that causes calcium and lanthanide ions to precipitate in the presence of fluoride, CaF_2 NPs or Ln-doped CaF_2 NPs readily form upon mixing the component ion solutions. The as-prepared NPs are typically pseudo-spherical and have diameters ranging from 10-20 nm (**Figure 3.2A**). Subsequently, the as-prepared NPs were annealed in a hydrothermal cell for 6 hours at 180 °C, which resulted in the formation of highly regular cubic nanocrystals; the overall mean diameter for a representative CaF_2 NP sample following annealing is 13.6 ± 3.5 nm (**Figure 3.2B**), still within the typical range of sizes before hydrothermal treatment. Evaluation of the elemental composition of the CaF_2 NPs via EDX measurements showed particle compositions close to the expected ratio of 1:2 calcium: fluorine in the undoped CaF_2 NPs (**Figure 3.3**).

	Sample	Ca Atomic %	F Atomic %	Dopant Atomic %	Doping %
B	CaF_2	30.54	64.38	--	0
	CaF_2:Tb	27.88	60.62	(Tb) 6.20	18.2
	CaF_2:Eu	29.52	58.72	(Eu) 5.56	18.8
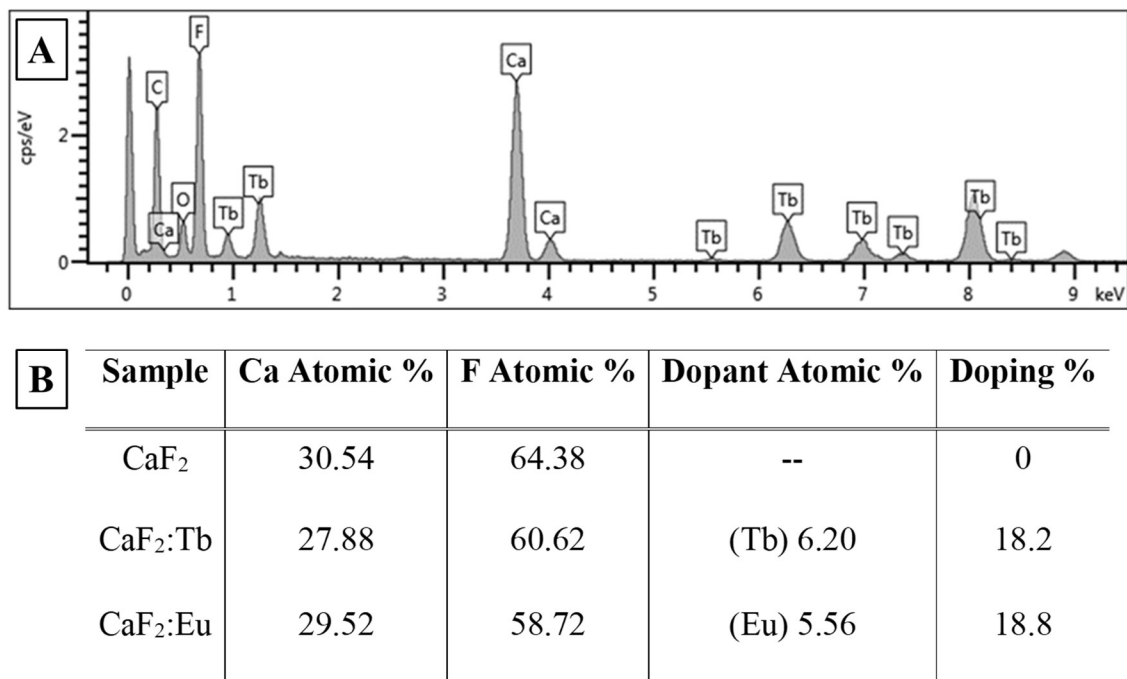
Figure 3.3) (A) EDX spectrum of CaF₂:Tb NPs and (B) EDX-derived % atomic compositions of CaF₂ NPs.

In comparison, when 15% of the calcium ions were replaced with either terbium or europium ions in the metal ion precursor solution, EDX measurements showed that the Ln ion accounted for approximately 18% of the cations in the resulting CaF_2:Ln NPs (**Figure 3.3B**). This % doping was targeted as it has previously been reported that doping beyond 15% in similar systems yielded diminishing returns of luminescence intensity.[35,40] By TEM, it was observed that the ~18% replacement of calcium ions with either terbium or europium ions did not significantly alter the typical diameters or morphologies of NPs; for example, a typical sample of CaF_2:Tb NPs after hydrothermal annealing (**Figure 3.2C, Table 3.2**) has a mean diameter of 13.4 ± 4.2 nm and is still somewhat faceted.

Table 3.2) Diameter data collected by measuring NPs with different doping qualities

NP Sample	Mean Diameter (nm)	Standard Deviation (± nm)
CaF_2	13.6	3.5
CaF_2:Tb	13.4	4.2
CaF_2:Eu	12.5	3.3

While hydrothermal annealing did not substantively alter the TEM-observable mean diameters of the NPs, changes in the crystallite size were observable by PXRD. PXRD patterns before and after hydrothermal treatment (**Figure 3.2D, E**) both reveal the expected diffraction pattern of the fluorite-type CaF_2 lattice; all peaks can be indexed to fluorite CaF_2 (PDF Card 35816), and there are no obvious crystalline impurities. Noticeable peak broadening is observed both before and after hydrothermal treatment, and the FWHM of the peaks can be used to estimate the crystallite size using the Scherrer equation. Before hydrothermal annealing, the NPs have a calculated mean diameter of 3.2 ± 1.8 nm, which increases to 10.2 ± 1.6 nm following annealing. The similarity between the PXRD-determined crystallite size and the TEM-measured diameter of the NPs post-annealing indicates that the annealed NPs are single crystalline, whereas they were likely polycrystalline before the treatment (Illustrated in Figure 3.4). It is, therefore, reasonable to conclude that the annealing treatment reduces grain boundaries within the as-prepared NPs, more so than it results in the ripening of the as-prepared NPs into larger particles.

Hydrothermal Annealing

Polycrystalline

Stainless Steel
Autoclave (180 °C)

Larger Crystallites
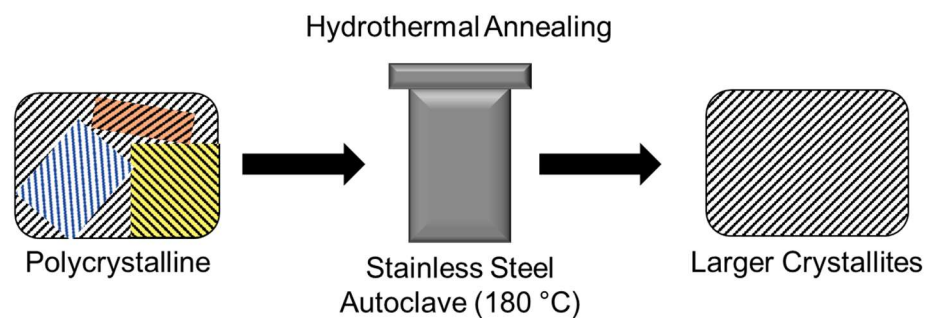
Figure 3.4) Illustration of the effect of hydrothermal annealing on crystallite size

Finally, in comparison of the PXRD patterns of Ln-doped vs. undoped CaF_2 NPs following annealing, it was observed that both the peak positions and the crystallite sizes are essentially the same at the ~18% level of Ln doping (**Figure 3.2F, G**); that is, the addition of Ln-dopant does not result in substantive structural or size changes in the product NPs.

3.3.1. *Influence of Crystallite Size on Lanthanide Ion Photoluminescence Intensity*
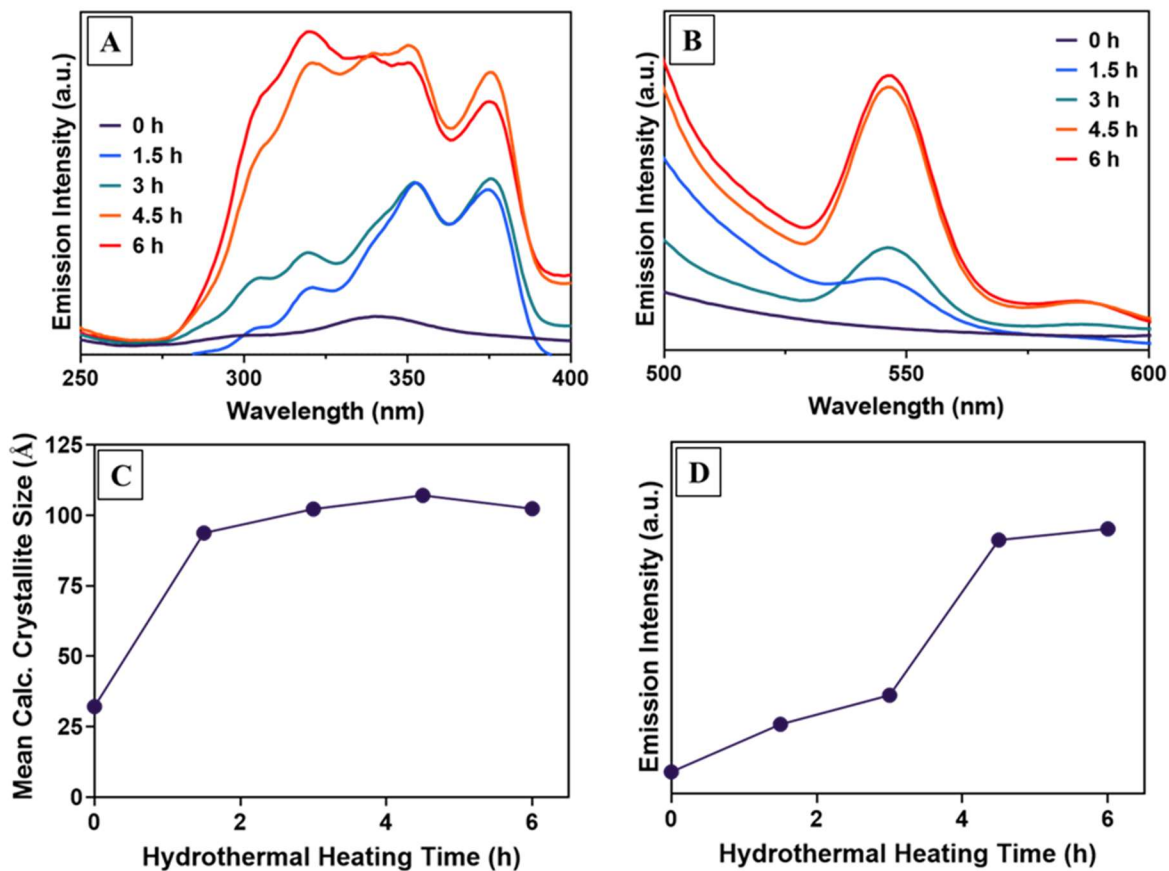
Figure 3.5) (A) Excitation spectrum of CaF$_2$:Tb NPs with variable hydrothermal annealing times, monitoring the intensity of the 545 nm emission. (B) Emission intensity of the samples when excited by 320 nm radiation. (C) Crystallite size data estimated from XRD patterns of each sample using the Scherrer equation. (D) Emission intensity at 545 nm plotted vs. increasing hydrothermal heating time.

The effect of the observed increase in crystallite size with annealing on Ln ion luminescence intensity was next investigated. Hypothesizing that increases in crystallite size would correlate with increased lanthanide ion emission intensity, photoluminescence excitation and emission spectra were monitored over time by removing aliquots of CaF$_2$:Tb NPs at different time points during the hydrothermal treatment For the Tb-doped CaF$_2$ NPs,

changes to the photoluminescent properties were observed by monitoring the Tb $^5D_4 \rightarrow {}^7F_5$ transition at 545 nm (**Figure 3.5A, B**); corresponding PXRD measurements were also performed on these aliquots, and crystallite size was estimated from line broadening (**Figure 3.5C**).
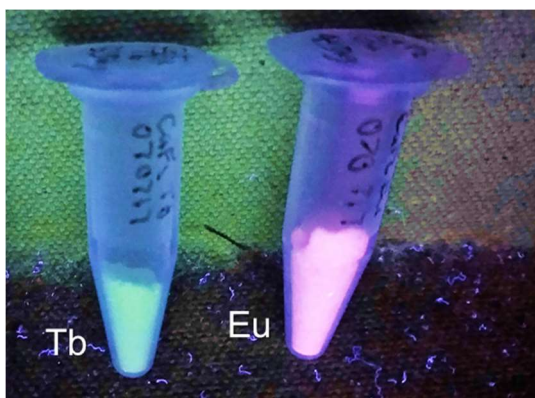
Figure 3.6) Photograph of CaF$_2$ NPs excited by 365 nm UV light

The as-prepared CaF$_2$:Tb NPs were observed to be only weakly photoluminescent, having low initial absorptivity across the 300-400 nm range, and negligible emission intensity in the visible region. With increased annealing time, absorptivity initially increased over the wavelength range 300-400 nm. At longer time points, increased absorptivity extended down to 275 nm (**Figure 3.5A**). These increases in absorptivity were well correlated with increased photoluminescence intensity in the visible region (**Figure 3.6**). For example, the increase in intensity at 545 nm, which was initially significant, is even more dramatic at longer annealing times as the absorptivity at shorter wavelengths increases (**Figure 3.5B**). Both the excitation and emission spectral changes plateau after 4.5 hours.

While the photoelectronic properties are observed to plateau only after 4.5 hours, by PXRD line broadening it was observed that the mean crystallite size no longer increased after 1.5 hours of hydrothermal treatment (**Figure 3.5C**); that is, the photoluminescence emission intensity continued to increase while the crystallite size did not (**Figure 3.5D**). The further increase in emission intensity with hydrothermal heating time (up to 6 hours) is most likely the result of the reduction in the concentrations of point defects within the CaF_2 matrices, leading to decreasing probability of non-radiative decay of the nanocrystal excited state at those sites and increasing probability of radiative decay at Ln-ion dopant sites.[41,42] One potential type of defect may be water molecules trapped in the crystalline lattice, made likely by the aqueous conditions in which the NPs are coprecipitated. Vibrations of the trapped water may lead to the loss of energy to heat within the crystal, reducing luminescence intensity. Other groups have presented similar hypotheses, however, the introduction of new defects that occur during irradiation has left water defects without extensive study.[43]

3.4. Mesoporous Silica Coating and Organosilane Surface Modification
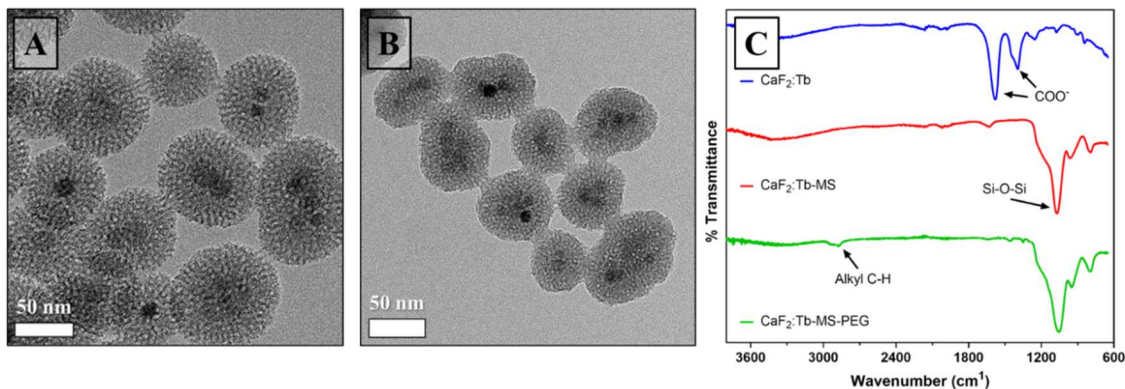
Figure 3.7) Surface modification of CaF$_2$:Tb NPs. TEM images of (A)CaF$_2$:Tb-MS NPs and (B) CaF$_2$:Tb-MS-PEG NPs.(C) FT-IR spectra of as-prepared CaF$_2$:Tb NPs (top), CaF$_2$:Tb-MS NPs (middle), and CaF$_2$:Tb-MS-PEG NPs (bottom).

Following successful synthesis of citrate-stabilized CaF$_2$:Ln NPs, a mesoporous silica (MS) coating was subsequently deposited on the NP surfaces to prepare CaF$_2$:Ln-MS NPs (**Figure 3.7A**). This MS coating was applied for several reasons. First, the as-prepared citrate-stabilized NPs were not easily redispersed as stable aqueous colloids, thus limiting their biological potential; we hypothesized that the MS coating would increase the hydrophilicity of the NPs to promote colloidal stability. Further, the MS coating provides the opportunity to covalently modify the NP surfaces with a wide variety of commercially available organosilane reagents, [44] thus permitting further synthetic alterations to increase colloidal stability and biological utility. Finally, mesoporous silica MS NPs on their own are popular biomedical agents due not only to their hydrophilicity but also to their ability to carry and release an encapsulated small molecule payload. Mesoporous silica NPs have

pores with sizes that are tailorable in synthesis, and as such, they have been studied as host vehicles in a variety of drug delivery, therapeutic and imaging applications.[21,22,45]

To prepare CaF_2:Ln-MS NPs, we modified a literature procedure used in the production of hollow mesoporous silica NPs, where relatively thin mesoporous silica shells were uniformly deposited onto solid silica cores that were later removed by selective structural etching.[46] First, the as-prepared CaF_2:Ln-MS NPs were dispersed in an aqueous solution along with cetyltrimethylammonium bromide (CTAB), to form a micellar solution upon rapid stirring. Next, tetraethoxysilane (TEOS) was added to the micellar solution, and the water solvent acted to initiate hydrolysis of TEOS to orthosilicic acid, and subsequent polycondensation of cross-linked silica onto the surfaces of the NPs. Due to surface-associated CTAB, small silica-coated cavities containing organic surfactant were formed in the silica shells deposited around the CaF_2:Ln NP cores. Subsequently, the silica-coated CaF_2:Tb NPs were isolated and further treated with a concentrated solution of hydrochloric acid in ethanol, which removed the CTAB and left mesopores in the deposited silica shell.

Following deposition of the MS coating, morphological evaluation of a sample of CaF_2:Tb-MS NPs by TEM revealed that occurrences of multiple CaF_2 cores in single MS shells were commonly observed and that isolated particles had an overall average diameter of 55 ± 9 nm (**Figure 3.7**). Since the overall average diameter is less than 100 nm, these NP constructs are potentially appropriately sized for use as intravenously administered agents. Further, in high-resolution images (not shown), ~2-3 nm diameter pores are observed in the silica shells, and these voids are large enough to enclose a variety of small

organic molecules. EDX analysis of the CaF_2:Tb-MS NPs shows that these structures are ~61% silica and 36% CaF_2:Tb by mass.

While mesoporous silica coatings on NPs are common in literature, applying a silica coating to a new NP system presents optimization challenges, including avoiding the aggregation of multiple NPs within single shells and self-nucleation of pure mesoporous silica NPs. While optimization is beyond the scope of this proof of principle synthesis and functionality assessment, we observed that the CaF_2:TEOS ratio was crucial to control the reproducibility of coating the CaF_2:Tb NPs while maintaining a significant mass % of CaF_2:Tb, which kept the NPs observably luminescent. Of the various ratios tested, 300 µL of TEOS to 54 mg of CaF_2 in a 110 mL water/ethanol system was found to be optimal for minimizing particle aggregation related to surface charge. Lower concentrations of TEOS resulted in CaF_2 without silica coatings, whereas higher concentrations of TEOS led to NP size increases due to coating thicknesses that would be prohibitive to cellular uptake or use as an RL agent.

3.4.1. Organosilane Surface Modification

Table 3.3) XPS-derived Atomic % concentrations measured from the surface of differently treated silica NPs

Conditions	Atomic % Si	Atomic % C	Ratio
Untreated Silica	17.5	37.3	1:2.1
Water/Triethylamine	8.5	31.7	1:3.9
Water/NH$_4$OH	9.0	45.7	1:5.1
Ethanol/ Triethylamine	11.8	38.1	1:3.2
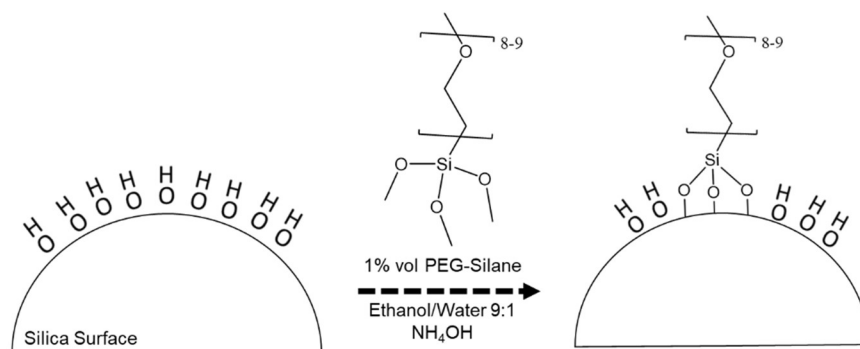
Figure 3.8) Graphic description of the process of PEG-silane attachment to silica surfaces.

PEG-silane was bound to the mesoporous silica to neutralize the charge of the NP, thus avoiding opsonization, or the aggregation of proteins which signal for an immune resonse, in biological systems while maintaining high hydrophilicity. To prevent opsonization, a very dense layer of PEG is desired[47–49], as the density of the PEG chains

on the surface affects the conformation that the chain takes and how effectively it shields the surface charge of the NP.[50] Surfaces treated with very high densities of PEG show a "brush" style conformation with the PEG extended far off the surface, straightened on its sides by other PEG strands. In lower-density environments, PEG collapses on itself in a "mushroom" morphology, which stays closer to the surface of the NP and is less effective at shielding surface charge. Further complicating the effectiveness of PEGylation is the binding force between PEG and the surface which affects the PEG's ability to gradually fall off, or "shed".[51] While this shedding reduces the density of the coating, it also removes proteins that have adhered to the NP and delays recognition by immune bodies.

Strongly basic conditions were used to ensure complete and rapid hydrolysis of the PEG-silane precursor, encouraging dense PEG layer deposition. This was done by dispersing the CaF_2:Tb-MS NPs in an aqueous solution with a catalytic amount of ammonium hydroxide and stirring at room temperature. XPS experiments were performed to confirm that aqueous conditions with a strong base attached the most PEG to the surface out of all of the conditions tested. CaF_2 is not compatible with the available VersaProbe XPS due to the XPS' LaB_6 electron beam generator. Commercially available silica NPs (Ludox) were used as a stand-in for the silica surfaces.

These conditions were tested amongst other combinations with weaker bases and anhydrous ethanol, and were found to attach the greatest amount of organic mass to the surface of the silica (Table 3.3). After PEG attachment, the NPs are collected into a pellet by centrifugation without sonication, then dried in a 60ºC oven overnight in a curing step. This step can encourage the attachment of weakly bound silanes to either the silica surface

or to each other by dehydrating the material, encouraging the dehydration condensation of the silanol groups on the silane and silica surface[52]. Additionally, DLS analysis revealed that CaF$_2$:Tb-MS-PEG NPs dispersed in millipure water have a mean hydrodynamic diameter of 299 ± 2 nm, PDI of 0.372 ± 0.016, and a zeta potential of -32.2 ± 0.473 mV.

The success of surface modification steps was validated by FT-IR spectroscopy, which was used to confirm the chemical identities of surface species for isolated NP products (**Figure 3.7C**). Before the addition of the mesoporous silica coating, the most prominent absorbances in the CaF$_2$:Tb spectrum result from COO- stretching vibrations, which can be attributed to the citrate used as a stabilizer during synthesis. After the addition of the silica coating, the Si-O-Si stretch becomes prominent at 1050cm^{-1}. Lastly, PEGylation of the CaF$_2$:Tb-MS NPs is supported by the presence of new alkyl C-H stretches at 2900 cm^{-1}, which can be attributed to the sp^3 C-H bonds of the ethyl groups in PEG. Taken together, these findings confirm that the CaF$_2$:Tb-MS-PEG NPs were successfully produced, and their radiological and biological properties are further examined in the following sections.

3.5. Radioluminescent Properties of CaF$_2$:Ln NPs

Photoluminescent CaF$_2$:Ln NPs have been studied by several groups in the fields of biomedical diagnostics and therapeutics,[39,53–55] as CaF$_2$:Ln NPs can act as a source of visible-range photons, similar to other types of NP which enable imaging within biological tissues.[56,57] The same emitted photons can also photocatalyze specific chemical reactions, producing toxic species to kill local cells in a process commonly known as (PDT). One of the most prominent applications of CaF$_2$:Ln NPs is in two-photon near-IR to visible energy

conversion for deep tissue diagnostic and therapeutic applications. However, X-rays have greater biological tissue penetration depth as compared to near IR radiation, and consequently, interest in radioluminescence (RL) applications of CaF_2 optical matrices has been stimulated.

While bulk CaF_2 and Ln-doped CaF_2 have been widely explored in RL applications, the RL characterization of doped CaF_2 nanomaterials is less common. The intrinsic RL properties of undoped CaF_2 NPs have been explored by Bezzera et al., who observed emission attributed to self-trapped excitons at 293 nm and from the F-centers at 428 nm.[58] Comparatively, Jacobsohn et al. investigated CaF_2:Eu NPs, where irradiation with a 40 kV X-ray source resulted in emission intensity at 420 nm, indicative of the presence of Eu^{2+}, as well as the expected Eu^{3+} emission transitions between 550-700 nm.[59] These studies illustrate that the RL properties of CaF_2 and CaF_2:Ln observed on the bulk scale are preserved in the nanoscale materials, which promoted our interest in exploring the potential of RL CaF_2:Ln NPs in biomedical X-ray imaging and therapeutic applications. The Eu^{3+} and Tb^{3+} -doped CaF_2-MS NPs we have synthesized in this work have potential in multiple, simultaneous medical modalities such as spatial imaging, drug or therapeutic delivery, or X-ray activated photodynamic therapy.
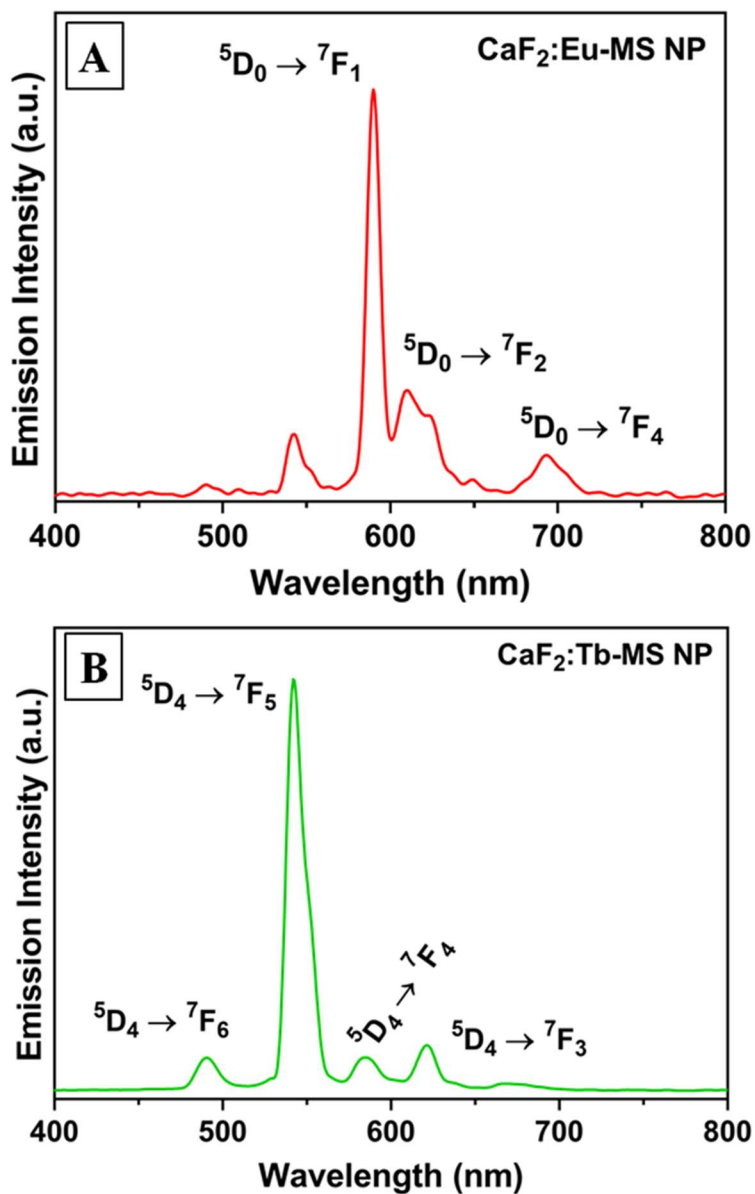
Figure 3.9) Radioluminescence emission spectra of (A) CaF$_2$:Eu-MS NPs and (B) CaF$_2$:Tb-MS NPs.

To assess radioluminescence, dry powders of CaF$_2$, CaF$_2$:Tb, and CaF$_2$:Eu were irradiated at 130 kVp using an X-ray irradiator and visible light emission in the 400-800 nm range was monitored using a fiber-optic spectrophotometer. Each type of NP was

assessed with and without the mesoporous silica shell. Expectantly, the undoped CaF_2-MS NPs did not produce visible radioluminescence under these conditions (**Figure 3.10**), as the self-trapped exciton transition of CaF_2 emits at too short of a wavelength to be observed with this RL measurement apparatus. In comparison, the lanthanide-doped CaF_2-MS NPs displayed bright radioluminescence upon X-ray excitation (**Figure 3.9**). The CaF_2:Eu-MS NPs exhibited distinct Eu emission peaks at 590 nm ($^5D_0 \rightarrow {}^7F_1$), 610 nm ($^5D_0 \rightarrow {}^7F_2$), 645 nm ($^5D_0 \rightarrow {}^7F_3$), and 693 nm ($^5D_0 \rightarrow {}^7F_4$), with the $^5D_1 \rightarrow {}^7F_2$ emission at 590 nm being most intense. Comparatively, The CaF_2:Tb-MS NPs displayed characteristic emission peaks at 490 nm ($^5D_4 \rightarrow {}^7F_6$), 542 nm ($^5D_4 \rightarrow {}^7F_5$), 586 nm ($^5D_4 \rightarrow {}^7F_4$), and 621 nm ($^5D_4 \rightarrow {}^7F_3$), of which the $^5D_4 \rightarrow {}^7F_5$ transition at 542 nm displays the highest emission intensity. We compared the RL of these samples to the as-synthesized CaF_2:Ln NPs, without the MS shell, and did not observe any significant spectral differences in the case of Ln = Tb (**Figure 3.10**). However, in the case of Ln = Eu, the MS shell addition introduced an emission at 540 nm, which is perhaps attributable to emissive defects in the silica, as emissions in this region have been previously observed upon silica's excitation with keV-scale irradiation.[60] The relative emission intensities are known to be informative as to the coordination of the Eu dopant ions within the fluorite crystal structure and the dominance of the $^5D_0 \rightarrow {}^7F_1$ transition at 591 nm implies that the dopants are replacing Ca^{2+} in the lattice.[61,62] Overall, these findings demonstrated the X-ray activation of lanthanide ion luminescence in the CaF_2:Ln-MS NPs, and we further assessed the CaF_2:Tb-MS NPs in cytotoxicology experiments, both in the absence and presence of incident X-radiation.
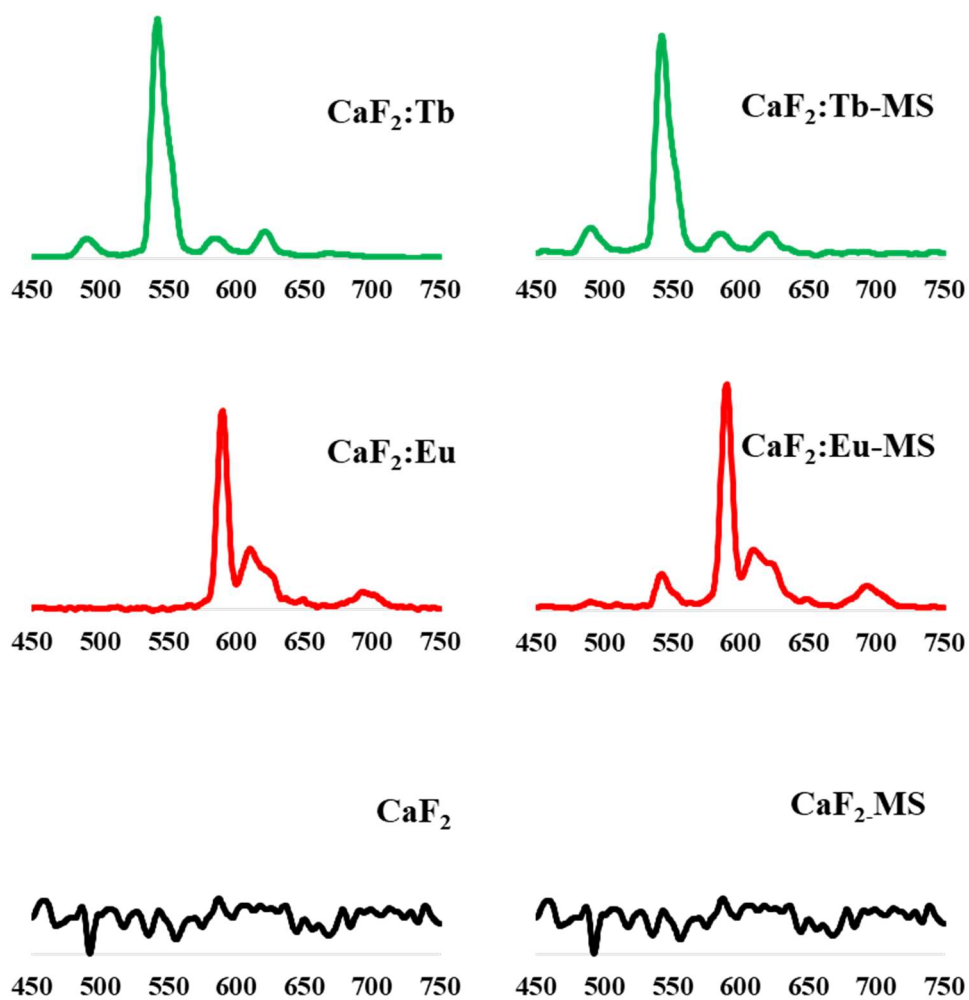
Figure 3.10) Comparison of X-ray luminescence spectra of doped CaF$_2$ NPs before and after coating with mesoporous silica.

3.6. Conclusions

This study has presented the synthesis of CaF$_2$- core mesoporous silica-shell NPs, and shown them to be applicable as RT enhancing materials. Details of the optimization of this synthesis have been discussed to aid decision-making for those who wish to replicate the work. The NP is X-ray luminescent and biocompatible under standard conditions. Once

X-ray radiation is applied, however, the NPs begin to generate hydroxyl radical which can enhance RT's killing of cells. Future work that could forward this application is the addition of ligands to the surface that would target the NP to specific types of tissues. Also, although physical enhancement has been explored here, the luminescence of the CaF_2 core could potentially be used to enable X-ray excited photodynamic therapy, which would have the advantages of the current NP construct while providing additional routes for radical production.

CHAPTER 4 - ASSESSMENT OF BISMUTH AND CALCIUM FLUORIDE

NANOPARTICLES FOR RADIOTHERAPY ENHANCEMENT

4.1. Introduction

The goal of the syntheses in the previous chapters was to produce two types of NPs capable of increasing cell death during RT. RT damages tissues by generating (ROS), either by exciting the electrons of cellular structures, or more likely, exciting the electrons in water molecules. These radicals and other excited species are highly reactive and can damage critical organelles to kill the cells or prevent their division.

We hypothesized that dense, inorganic NPs can efficiently attenuate and convert high-energy X-rays to produce multiple lower-energy photons, thus multiplying the number of ROS generated during irradiation. In this chapter, we measured and compared the RT enhancement ability of Bi and CaF_2:Ln NPs. The NPs were assessed for their radiolytic capabilities and biocompatibility using spectroscopic assays, an *in vitro* assay, and in the case of the Bi NPs, an *in vivo* assay. In the spectroscopic assays, selective fluorescent probes for singlet oxygen and hydroxyl radical have been used to quantify ROS production under X-ray irradiation in the presence of NPs, as compared to irradiated samples without NPs. *In vitro* assays have been performed to assess the viability of cells incubated with NPs in the presence or absence of X-ray radiation. In these experiments, a desirable result would be that the NPs would have negligible cytotoxicity unless radiation is applied, and in the presence of radiation, co-treatment with NPs and RT would kill more cells than RT alone. For the CaF_2:Tb platform only, the use of Rose Bengal was additionally investigated as an added photosensitizer to possibly increase singlet oxygen

production via RT. Finally, a preliminary *in vivo* experiment was performed to assess the biodistribution of Bi-DSPE-PEG NPs in mice and identify potential means of clearance.

4.2. Experimental

4.2.1. Reactive Oxygen Species Production Assays

Stocks were prepared of various NP constructs with fixed concentrations of 1 µg/mL in water. Each dispersion was sonicated for at least 5 minutes. These dispersions were plated into 96-well plates, 100 µL per well. Some wells received millipure water instead of NP solutions as a control. At this time, to each well was added either 10 µL of a 10 µM aminophenyl fluorescein (APF) solution or 10 µL of a 10 µM singlet oxygen sensor green (SOSG) solution. These plates were transferred to a Faxitron Cellrad small animal X-ray irradiator and irradiated at 130 kVp and 20 mA for variable amounts of time to attain different radiation doses. Once the radiation exposure equated to a predetermined dose, some samples were removed from the irradiator and pipetted into a separate 96 well plate. Solutions remaining in the well plate could then continue to be irradiated. Immediately following X-ray irradiation, the aliquots in the 96 well plates were analyzed by fluorescence measurements using a plate reader. APF fluorescence intensity was measured using an excitation wavelength of 490 nm and was monitored at 520 nm, and SOSG fluorescence intensity was measured using an excitation wavelength of 500 nm and monitored at 525 nm.

4.2.2. In Vitro Assays

Cells of various lineages were cultured in appropriate growth media through at least 3 passages between being thawed and being used. Media selection followed recommendations from the American Type Culture Collection. Cells were plated into 96-well plates at a density of 10,000 cells per well. After waiting an appropriate time for cells to affix to the substrate, media was replaced with NP-dosed media or non-dosed control media where necessary. The cells were then incubated in the media for a period of time, the length of which varied with the cell line. After the incubation period, new media was placed over the cells, and then cells were irradiated at 130 kVp via a Faxitron CellRad cell irradiator until 4 Gy of radiation was delivered. Cells were then cultured for another 24 hours. Media was then replaced with new media containing 10% vol/vol Alamar Blue. After a set metabolizing period which varied from 2 to 4 hours with cell line, well plates were moved to a plate reader, and the fluorescence intensity of metabolized Alamar Blue was read for each well using an excitation wavelength of 530 nm and monitoring emission at 590 nm. Different conditions included untreated cells, cells treated with variable doses of NPs, cells treated with RT, and cells co-treated with variable doses of RT and a fixed dose of RT. The experimentally determined fluorescence intensity values for cells treated with various doses of NPs in the presence or absence of X-ray radiation were normalized to that of cells not treated by NPs or X-ray radiation.

4.2.3. CaF$_2$-MS NPs Rose Bengal Loading

15 mg of mesoporous silica-coated CaF$_2$:Ln NPs were suspended in 20 mL of an aqueous 10 mM Rose Bengal solution with sonication in a 100 mL round bottom flask. The dispersion was stirred at room temperature for 2 hours. Then, 40 µL of ammonium hydroxide (30%) was added, then 100 µL of PEG-silane. This solution was stirred at room temperature for two hours. The reaction was poured into a centrifuge tube, and 10 mL of ethanol was added to flocculate the NPs. Solids were collected by centrifugation before undergoing resuspension in 10 mL of 1:1 water: ethanol and centrifuging. This was repeated two additional times with water followed by 2 more cycles of redispersion and centrifuging with 10 mL of ethanol. The solids were dried at 50 °C overnight before being gently powdered with a spatula.

4.2.4. DSPE-PEG Addition onto Bi NPs

10 mg Bi NPs with polyvinylpyrrolidone-graft-triacontane coatings was dispersed in 10 mL of chloroform through 30 minutes of sonication. In a separate container, 10 mg of DSPE-PEG was dissolved in 10 mL of chloroform through shaking. The two solutions were combined in a 500 mL flask and stirred for 10 minutes. The flask was placed on a rotary evaporator and chloroform was slowly removed from the system. The bath temperature was kept at 30 °C, system pressure at 300 mbar, and rotation speed at 150 rpm. After 20 minutes, no more liquid was observed. The pressure of the system was adjusted to 50 mbar for another 10 minutes to remove residual chloroform. The dried NPs were redispersed in 10 mL of 1X PBS buffer with 30 minutes of sonication, then unconjugated DSPE-PEG was removed with two cycles of filtering through 100k MW centrifuge filters

followed by resuspension in PBS. After the final resuspension of the Bi NPs in 2 mL of PBS, the concentrations of these stocks were determined by ICP-MS analysis.

4.2.5. In Vivo Biodistribution

Balb/c mice (Charles River Laboratories) were injected via tail vein with 100 uL of Bi-DSPE-PEG NPs at a concentration of 1.5 mg/mL, resulting in a dose of 0.15 mg per mouse. Mice were observed for distressed or pained behaviors hourly for 8 hours after injection. Three mice were sacrificed via CO_2 asphyxiation after 24 hours, while one was sacrificed after 48 hours. Organs were collected from the mice after death, then homogenized, digested in nitric acid, and analyzed for bismuth content by ICP-MS.

4.3. ROS Production Assay Results

Before addressing the utility of Bi-Silica-PEG NPs and CaF_2-MS-PEG NPs in biological environments, solution spectroscopy assays were performed to probe their ability to increase ROS production during irradiation. The two probes used in this study were Aminophenyl fluorescein (APF) and Singlet Oxygen Sensor Green (SOSG), which become strongly fluorescent when they react with hydroxyl radical or singlet oxygen, respectively (**Figure 4.1**). Both APF and SOSG are fluorescein derivatives with a "deactivator" moiety initially bound to the fluorescein moiety. This deactivator reduces the compounds' fluorescence intensity, but can be altered or cleaved off such that fluorescence can be restored. In the case of APF, reaction with hydroxyl radical to cleave off the aminophenyl group is highly favorable and leaves a fluorescent compound. SOSG features an anthracene moiety as a deactivator. While the anthracene is involved in the extended pi

system of the fluorescein, it reduces fluorescence intensity. Upon reaction with singlet

oxygen, however, that is negated, and fluorescence is restored.
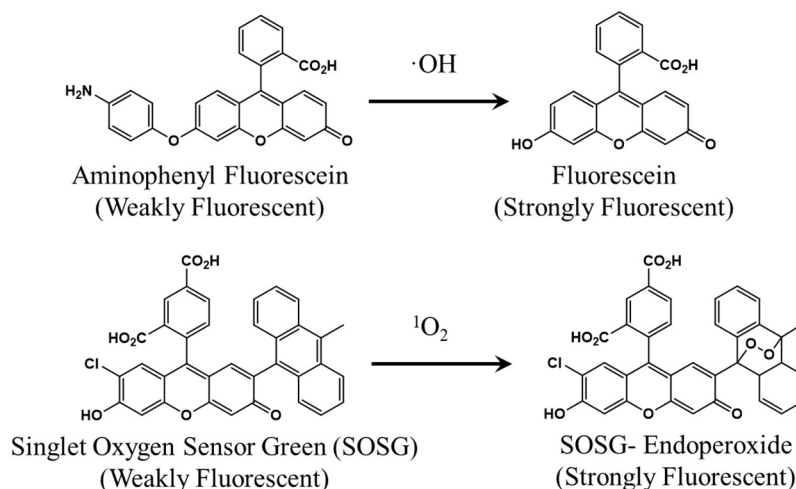
Figure 4.1) Reactions of reactive oxygen species probes with corresponding reactive oxygen species

In these experiments, solutions containing the fluorescent probes were irradiated

with various doses of 130 kVp X-rays. The fluorescence intensity of the probes was then

measured and can be correlated to the amount of ROS produced during irradiation. The

experiment was repeated in 1 µg/mL dispersions with various NP types. In the case of the

Bi-Silica-PEG NPs, only the complete construct was assessed. For the CaF_2-cored NPs,

CaF_2:Tb NPs and MS NPs were tested alongside the final CaF_2:Tb-MS-PEG NP to

determine the contribution of each component to ROS production. The results of these

assays are presented in **Figure 4.2**.
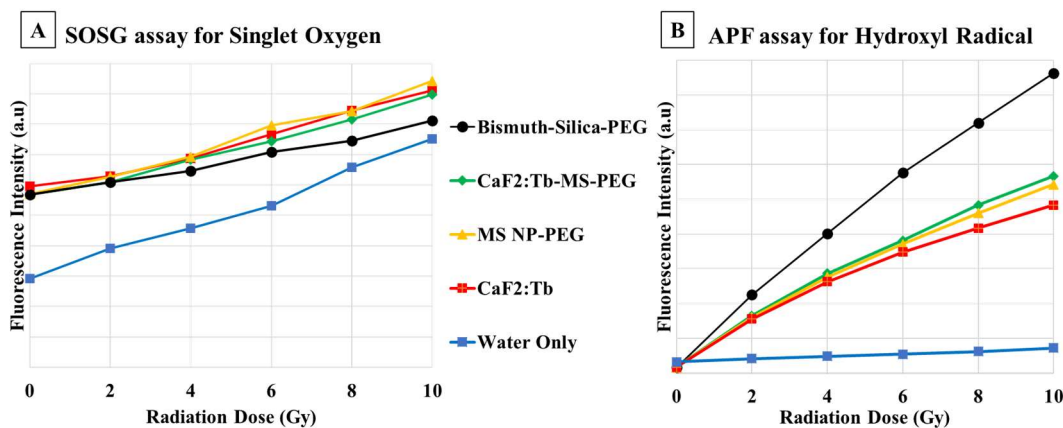
Figure 4.2) Results of Reactive Oxygen Species production assays with various NP constructs

In analyzing the data taken from these radical-reactive probes, the slopes of the curves represent the critical value of how many of a certain ROS are being produced per set dose of radiation applied to a sample. Compared to water alone, a steeper slope indicates more efficient production of ROS in the system. The slopes of the curves for NP-dosed solutions are less steep than water alone in the SOSG assay (**Figure 4.2A**) indicating that no tested NPs significantly increased the singlet oxygen produced per Gy of radiation. While the initial intensity of the SOSG probe is slightly higher in the presence of NPs, the singlet oxygen production per Gy of radiation is reduced for all NP dispersions than water only. The presence of these NPs appears to inhibit singlet oxygen formation, rather than amplify it. Given the lack of suitable photosensitizers, this is reasonable. The generation of singlet oxygen is typically induced with specific energy pathways that produce near-IR photons capable of exciting triplet O_2 to its singlet state. Section 4.5 details efforts to attach Rose Bengal to the CaF_2 NP such that this type of energy pathway could be realized.

More significant findings are found in the assessment of hydroxyl radical production (**Figure 4.2B**). Compared to water alone, all NP-dosed solutions showed greater rates of hydroxyl radical production per Gy of radiation. Bi-Silica-PEG NPs produced hydroxyl radicals the most efficiently, followed by the CaF_2:Tb-MS-PEG, MS NP-PEG, and CaF_2:Tb NPs which performed similarly to each other. The differences in the enhancement of hydroxyl radical production can be attributed to two prominent differences between the NP types, density and atomic number. The 55 nm bismuth cores used in the Bi NPs are the largest, densest (9.78 g/cm^3), and highest Z material ($Z = 83$) among those tested. The denser, higher -Z Bi NPs were the most likely to initially scatter an X-ray. In addition, their greater volume made it more likely to divide the energy of the incident X-ray multiple times before the energy was allowed to escape the bismuth crystal volume, creating multiple excited states that can generate radicals. This was less likely in the 12 nm CaF_2:Tb cores of lesser density (3.18 g/cm^3) and lesser average atomic number (average Z by mass=26.8). Another interesting comparison is between CaF_2:Tb and MS-PEG NPs. While MS has a lesser density than CaF_2:Tb, it still produced more hydroxyl radicals throughout irradiation. The MS NPs are larger in volume, which may contribute to the effect, but much of their volume is filled with water, making it hard to predict how excited states and low energy photons would be scattered and absorbed in the structure. Silica has been studied for its ability to generate radicals on its surfaces, which may have provided another route for this effect.[17,63]

All NP types increased the number of hydroxyl radicals produced per Gy of radiation, meaning that they all could enhance the cell-killing ability of RT. The

CaF$_2$:Tb-MS-PEG produced the greatest number of radicals throughout irradiation out of all CaF$_2$ constructs tested, leading to its continuance in further application testing. The visible photon emission from this NP allows for other modalities and may be explored further in the future.

4.4. *In Vitro* Assays

4.4.1. *Assessing Radiotherapy Enhancement with NPs*

To assess the NPs abilities to enhance cell killing during RT, cells were dosed with variable concentrations of NPs and irradiated. Twenty-four hours after irradiation, cell viability was assessed using the alamarBlue assay. This assay measures the metabolic activity of a cell population, which can be correlated to the fraction of living cells. Due to the ROS-multiplying effects observed in the ROS generation assays, it was initially hypothesized that the presence of NPs would decrease the number of cells that survived RT, and that an increasing concentration of NPs would increase the degree of enhancement.
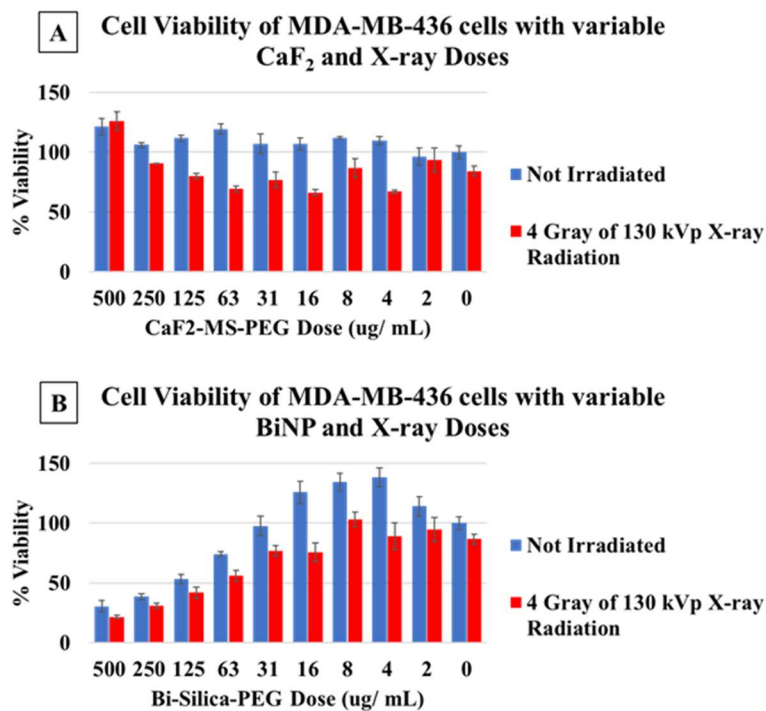
Figure 4.3) Results of viability assays to assess biocompatibility and RT enhancement in the presence of NPs

In experiments assessing CaF$_2$-MS-PEG NPs, the NPs were found to be well tolerated across all tested concentrations, with cell viability remaining near 100% at all tested doses (**Blue columns, Figure 4.3A**). However, once radiation was applied (**Red columns, Figure 4.3A**), some concentrations of NPs between 16 and 125 μg/mL were found to significantly enhance cell death, as evidenced by a drop in cell viability of the irradiated cells as compared to the non-irradiated control samples. Some conditions led to mean % viabilities above 100%, which may be attributed to NPs interacting with cells and possibly increasing their metabolic or proliferative rate above that of the control population. Whereas RT in the absence of NPs decreased cell viability by 16%, some doses of NPs decreased viability by 41% (at 16 μg/ml). While this aligns with the hypothesis of

the experiment, the increased cell death did not occur in a consistent trend with increasing concentration of NPs. Enhancement of cell killing was greatest at 63 µg/ml at 50%, but higher concentrations of 250 and 500 µg/mL showed little or no enhancement. Potential reasons why this occurs could be due to the interaction of high doses of NP with the cell walls, possibly preventing uptake. Future experiments to probe this limitation may include loading the MS shells of the NPs with a UV-fluorescent dye, then imaging single cells under UV excitation to correlate emission intensity with the location of the NPs. This may provide information as to how likely the NPs are to be internalized or adhere to the cell membrane.

The same experiment performed with Bi-Silica-PEG NPs provided significantly different results in terms of cytotoxicity. Without radiation (**Blue columns, Figure 4.3B**), increasing doses of Bi NPs showed some cytotoxicity, with doses of 63 µg/mL causing cell viability to drop to 74%. This did not support the hypothesis that the NPs were inherently cytocompatible, as significant decreases in cell viability should not have occurred without radiation. Despite this, further decreased cell viability during RT was observed (**Red Columns, Figure 4.3B**), and most significantly reduced cell viability from 126 to 76% when a 16 µg/mL dose of NPs was applied. While the presence of Bi-Silica-PEG NPs decreases cell viability in all doses, this decrease is not dose-dependent, further providing support for the null hypothesis.

Given the radical production assays of these species, interesting comparisons can be drawn. The ability of Bi NPs to enhance radiation damage to cells appears to be more significant at low doses, however, the cytotoxicity of the platform in its entirety is

deleterious. The CaF$_2$ NPs, however, are remarkably well-tolerated and show little cytotoxicity even at very high doses, although their enhancement of RT is not as great as Bi-Silica-PEG NPs. While the enhancing ability of the NPs seems to be in line with the well-characterized physical characteristics of their materials, the cytotoxicity of the NP Bi-Silica-PEG NPs will require extensive study to find its source. After these studies, a conclusion was drawn that the generally well-tolerated CaF$_2$ NP platforms were promising but should be modified to make their RT enhancement more pronounced.

4.5. Modification of CaF$_2$:Tb-MS-PEG NPs with Rose Bengal

Due to previous promising results in the enhancement of RT, improvement to the CaF$_2$:Tb-MS-PEG NPs was attempted with the addition of Rose Bengal (RB) which could provide a means of generating singlet oxygen. The attachment of RB was done by electrostatic attraction between the RB and MS layer before PEG was attached to the surface. Further optimization of the RB loading was not achieved within the timeframe of this study, however, the RB concentration in the NP was determined using UV-Visible spectroscopy. Measurements of known concentrations of Rose Bengal were plotted on a calibration curve before a sample with a known mass of RB-loaded NPs was measured. This experiment indicated that the RB was approximately 5% of the total NP mass, which was believed to be sufficient for the study.
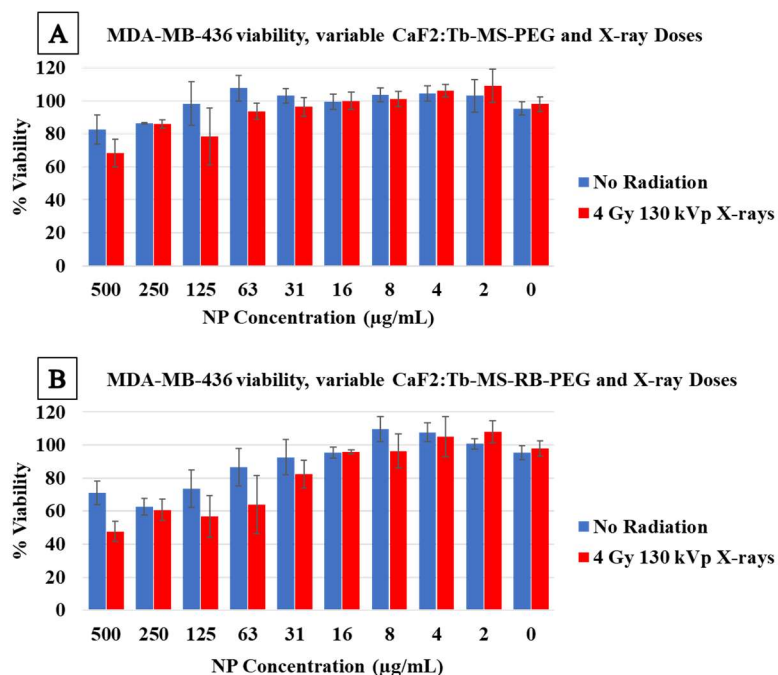
Figure 4.4) Cell Viability assays performed on CT26 NPs, assessed without Rose Bengal loaded (A), and with Rose Bengal Loaded (B) as well with or without X-ray RT

In vitro experiments with RB-loaded NPs displayed some cytotoxicity with RB present as well as a minor improvement of RT enhancement (**Figure 4.4**). This differed from previous cell viability experiments displayed in Figure 4.3, which may be a result of using a different cell line. While non-RB loaded NPs showed RT enhancement of 14% at 62.5 µg/mL, the presence of RB increased this to 17%. The greatest difference between non-loaded and RB loaded enhancement occurred in the highest measured NP dose, with unloaded enhancement at 14% and loaded enhancement at 23%. However, at this point, the cytotoxicity of the RB-loaded NPs had reduced the non-irradiated NP viability to 71%, which is not favorable for the intended application. There are two likely explanations as to the nature of the cytotoxicity observed with RB addition. The first is that the RB is leaking out of the NP, and is toxic to the cells, however, its low concentrations in solution act

against this explanation. The second is that the electrostatic loading of the RB onto the MS surface may interfere with PEG attachment in the subsequent synthetic step, which would lead to a less neutralized surface charge and some observed cytotoxicity. Further experiments assessing the rate of leakage of RB from the NP or the cytotoxicity of RB alone could support or deny these possibilities. Overall, the inclusion of RB into the NP did not drastically improve RT as was hypothesized, although small improvements were observed. To address why this occurred, experiments were performed with ROS probes (**Figure 4.5**).
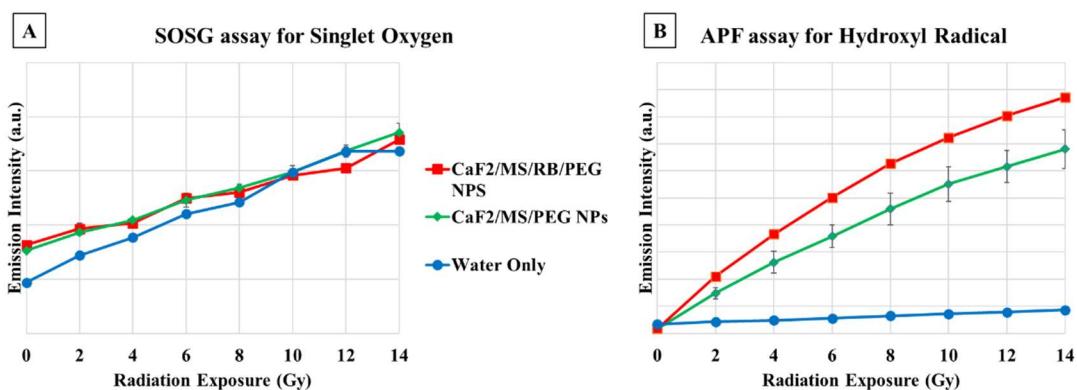
Figure 4.5) ROS assays performed on CaF$_2$-MS-PEG NPs with and without Rose Bengal. A) SOSG assay for singlet oxygen. B) APF assay for hydroxyl radical

These ROS generation experiments further supported the null hypothesis that RB was not effectively generating singlet oxygen. The SOSG assay showed no significant difference in SOSG produced per Gy of radiation between CaF$_2$-MS-PEG NPs with or without RB (**Figure 4.5A**). An unexpected finding was that the presence of RB increased the production of hydroxyl radicals (**Figure 4.5B**). Mechanisms in the literature which

could explain this phenomenon are scarce, and typically involve metallic catalysts, and so this cannot be explained at this time.[64]

4.6. Shortcut Surface Modification

Before the silica coatings presented earlier in chapters 2 and 3 were complete, an opportunity arose to perform some preliminary Bi NP biodistribution experiments in mice. The hydrophobic Bi NPs produced by the initial core synthesis were modified with DSPE-PEG, which anchors itself into the hydrophobic alkyl chains on the surface of the Bi NPs while presenting a PEG chain outward. The resulting NPs were highly hydrophilic and stable in PBS indefinitely. DLS data showed individually dispersible NPs with hydrodynamic sizes of 162 ± 24 nm and a zeta potential of -19 mV, meaning that their surfaces are nearly neutral and would not immediately collect a protein corona in the bloodstream. To have a coating provide a neutral surface charge while also dispersing the dense Bi NP in water was valuable, but this type of modification was prohibitively expensive and only used for preliminary biodistribution experiments.
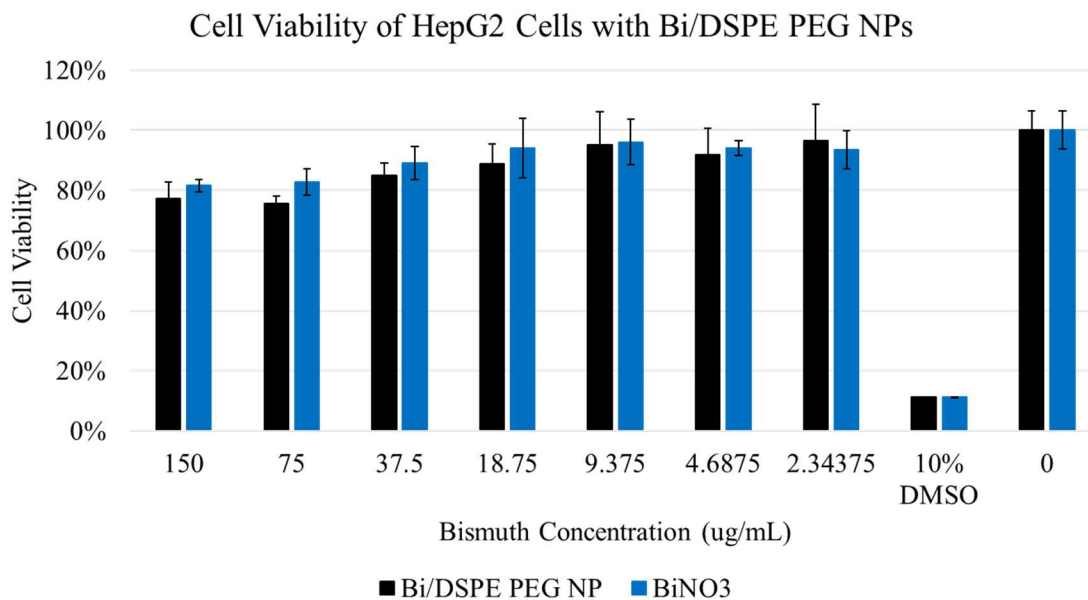
Figure 4.6) Cell viability data of HepG2 cells exposed to Bi-DSPE PEG NPs and BiNO₃ over 24 hours

The resultant coating on the Bi NPs rendered them highly biocompatible when cell viability was assessed in HepG2 cells (**Figure 4.6**). With the maximum bismuth concentration of 150 µg/mL, % viability was calculated to be 78%. As there is little literature on the cytotoxicity of bismuth ions alone, equivalent bismuth concentrations were tested with bismuth nitrate as well. Neither bismuth ions nor Bi NPs were prohibitively toxic, and matching concentrations of the two species showed similar trends in % viability. These preliminary assays supported the DSPE-PEG's effectiveness and permitted *in vivo* studies to proceed.
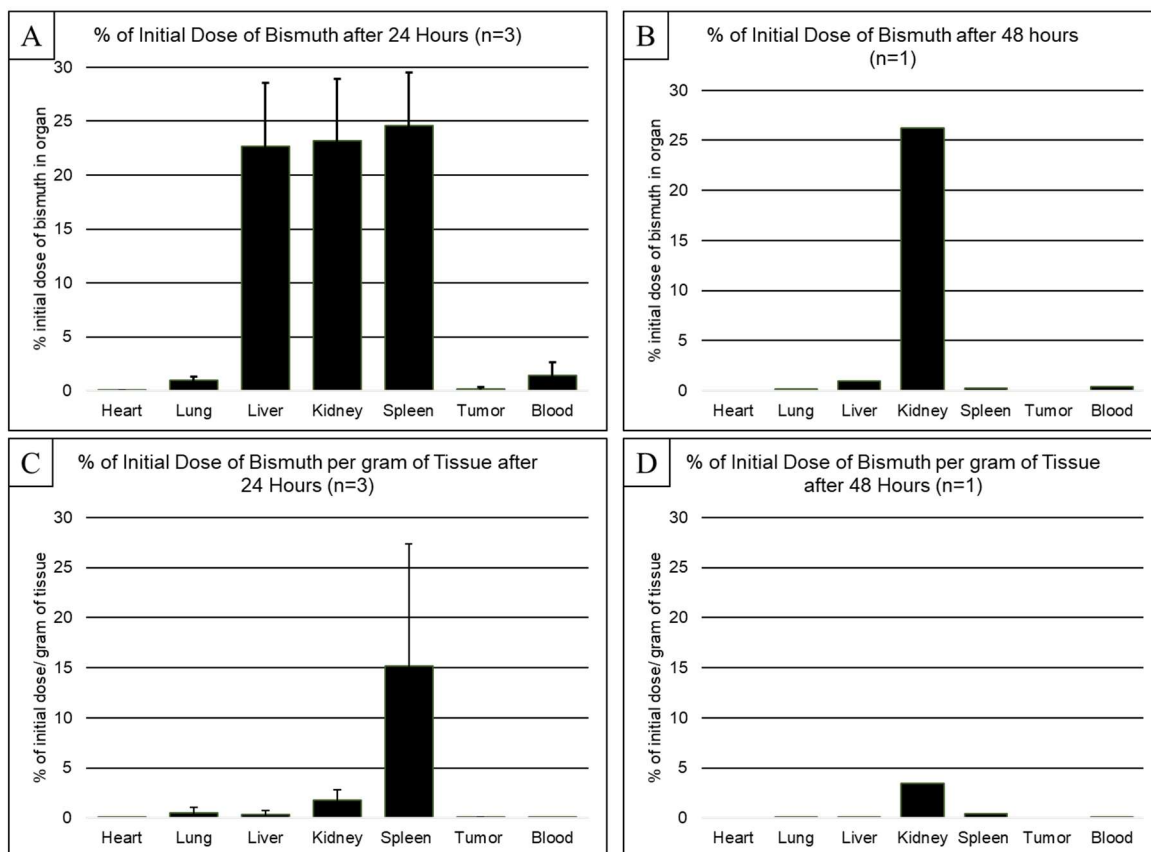
Figure 4.7) Preliminary biodistribution data of Bi NPs injected into the tail veins of mice.

4.7. Preliminary *In Vivo* Biodistribution Testing:

Initially, a single mouse was dosed with Bi NPs via tail vein injection and monitored over 48 hours for signs of distress that would require immediate euthanasia. Three more mice were then given the same treatment and monitored over 24 hours. Mice were sacrificed with CO_2 asphyxiation after the observation periods were complete, and their organs were homogenized into a slurry, digested with nitric acid, and analyzed with ICPMS for bismuth content. Results from the biodistribution experiments showed that the bismuth accumulated in the liver, spleen, and kidney of the mice at the 24-hour timepoint. (**Figure 4.7A**) While the high accumulation in the liver and spleen were expected, the

accumulation in the kidney was not as the Bi NPs had hydrodynamic radii that should have been too large for renal clearance.[16,65] Furthermore, the one mouse that was sacrificed after 48 hours (**Figure 4.7B**) shows a decreased concentration of bismuth in the liver and spleen and steady concentration in the kidney.

Further analysis of the % of the initial dose per gram of tissue provides information on the degree of bismuth accumulation in each tissue type. After 24 hours, the highest concentrations of bismuth were found in the spleen (**Figure 4.7C**). This mean spleen concentration has a high degree of error due to the similarly high concentrations of bismuth in each spleen combined with dissimilar masses. While the high total amounts of bismuth found in the kidneys (**Figure 4.7A,B**) may suggest renal excretion, the high concentration of bismuth found in the spleen at 24 hours, followed by the reduced concentration at 48 hours, suggests that fecal excretion is the more supported clearance route (**Figure 4.7C,D**). This aligns with what is generally accepted about NP clearance in relation to NP size.[65] To probe the clearance route most directly, future biodistribution experiments would require feces and urine collection for ICP-MS analysis along with organ tissues.

These experiments must be repeated with a significant sample size, however, this preliminary study may suggest that the NPs are degrading and leaving the liver and spleen to be renally excreted as species with smaller sizes. This finding would be of the highest significance, as it provides an advantage over other high-density NPs like gold which can serve the same purpose in RT enhancement but are inert in biological conditions. One matter that must be addressed in future work is the effect of the silica shell on the biodistribution and degradation of Bi NPs. Silica has been shown to degrade in biological

conditions, but at a much slower rate than that of bismuth in this set of experiments.[16,66] Also, the inclusion of targeting agents will be necessary for the development of this platform's usefulness as the data shows that the Bi NPs did not significantly load into the tumors to the point that RT is likely to be enhanced.

4.8. Conclusions

The Bi NPs and CaF_2 NPs presented in this thesis have both been used to enhance the damage done to a population of cells throughout RT. The materials' effectiveness in doing so is noticeably related to the physical characteristics of the materials, most notably their density. Attempts to improve the lesser ability in CaF_2 by attaching Rose Bengal were not successful, as the attachment of the RB demanded extensive iteration to make it functional with maintaining the biocompatibility of the material. While the highly-dense Bi NPs showed an aptitude for physical enhancement, the surfaces used to make them biocompatible were too rudimentary to allow for their silica-coated use. However, the safety of the core *in vivo* was assessed and supported in mouse models, and preliminary data suggests that their clearance time makes them a promising alternative to the biologically inert heavy metals.

CHAPTER 5 - CONCLUSIONS

In this thesis, NPs were synthesized with the purpose of increasing the killing of cancerous cells during RT while sparing nearby healthy tissues. Inorganic NPs, with their high densities and atomic numbers, are well suited for this task, as they interact with X-ray in such a manner as to localize the energy of the photon in the local environment. Novel syntheses of Bi NPs and CaF_2-MS NPs were developed and rigorously assessed through surveys of important parameters and optimization. Then, these NPs were used in RT enhancement experiments. The overarching hypothesis of these experiments was that the NPs would not be innately cytotoxic until struck with X-ray radiation, upon which they would multiply the number of ROS produced by the radiation and increase the number of cells killed by this treatment. The NPs synthesized in this work are effective payloads that are useful to multiply the production of radicals during RT, however, future work to improve their biocompatibility and biodistribution to select treatment sites will be necessary to create working therapeutics.

5.1. Bismuth Nanoparticles

Bismuth NPs have many favorable traits that make them promising as RT enhancers, most notably their high density and sparsely reported biodegradability. In this work, Bi NPs were synthesized from an alkylammonium iodobismuthate, a precursor with distinct advantages over others in the field. The reaction can be performed in air, as opposed to the strictly air-free conditions needed for other preparations. Pyrophoric materials used at high temperatures are also unnecessary. The NP products are single crystals with average diameters of 55 nm, which places them within the size range for

intravascular agents. After the core synthesis, they were coated with silica to produce a smooth, minimally thick shell that provides a reactive scaffold for the attachment of a variety of surface species.

However, with these advantages come limitations. The size of the Bi NPs is limited, as the reaction has multiple stages and conditions must be optimized for iodobismuthate formation as well as NP nucleation. To address these issues with the synthesis, there are some potential practical solutions. First, recalibration of the synthesis in a more conventional high boiling solvent, like dodecane, would address the issues found in the variation between solvent batches from a chemical supplier. The diisopropylbenzene used in this study was technical grade, which is convenient, however technical grade materials may have a higher degree of batch-to-batch variation in impurities which can affect a delicate NP synthesis. With that being standardized, more fine-tuning could allow the synthesis to reproducibly produce a range of sizes of uniform NPs, which would be advantageous when optimizing the characteristics of an intravenous agent.

Once a synthesis of Bi-Silica-PEG NPs was finalized, it was assessed for its ability to enhance radiotherapy. Biocompatibility testing showed the moderate tolerance of cells for these NPs, however, it proved to be toxic at high concentrations. Despite this, *in vitro* RT assays showed that the presence of the NPs significantly increased the killing of cells, supporting the hypothesis which motivated their synthesis. The benefits of the effect were offset by the issue of dose-dependent cytotoxicity even before RT was applied. Other Bi NP constructs, such as Bi-DSPE-PEG, did not display this cytotoxicity, suggesting that the bismuth core itself may not be the problematic component. To address this gap in

knowledge, a more thorough set of cytotoxicity experiments could be performed featuring Bi-PVP, Bi-Silica, and Bi-Silica-PEG NPs. This may provide information as to which step in the surface modification of the NP introduces a cytotoxic compound, and allow an alternate compound or synthetic step to be chosen and explored.

With DSPE-PEG coated Bi NPs, *in vivo* biodistribution assays were performed to assess if the size of the NP and oxidation rate of the Bi core would allow circulation and clearance. Time points of 24 hours showed bismuth collected in the liver, spleen, and kidneys, which changed to just the kidneys after 48 hours. As the whole NPs were too large to be filtered renally, these early results support that the NP can be oxidized and then cleared renally.

Future work on the Bi NP platform should take advantage of the silica shell optimization, but address the cytotoxicity that appears to come with it. While the DSPE-PEG-coated NP was effective in the *in vivo* experiments, the structure is held together by London dispersion forces that are less reliable than the covalent bonding strategies allowed by silane modification. These issues are compounded by the precision and cost that comes with executing DSPE-PEG coating, preventing scaling and extensive testing. As for improving the biocompatibility of the silica coating, the PEG chain length may be a factor to address. The DSPE-PEG chain had a molecular weight of 5000, while that on the PEG-silane was only 1000. Prevalent literature suggests that the former is more ideal for biological conditions.[67]

Besides optimizing PEG chain length, attaching not only PEG but also targeting ligands would allow the NP to be targeted to specific tissues; a necessity for use as an

intravenous agent. The attachment of this ligand would be a complicated task. It could be done by using a combination of PEG silane and aminosilane to decorate the surface of the NP with not only PEG, but primary amines. Attachment of the targeting ligand to these amines on the surface would likely not be successful, as it would be buried by the PEG layer and intangible to cellular membrane components which they must interact with. The ligand would have to be presented outside of the PEG layer by a spacer moiety, perhaps a long, linear, bifunctional molecule. A synthetic strategy of attaching the ligand to the spacer, then the spacer to the NP surface is the most likely to be successful.

5.2. Calcium Fluoride NPs

In this work, various preparations of nanomaterials have been adapted to produce a calcium fluoride core- mesoporous silica shell NP with several attractive features for RT enhancement. The CaF_2 core is much denser than tissue and can scatter X-rays effectively. The core can be doped with terbium or europium, enabling X-ray activated fluorescence with either green or red emission. This would be useful to either locate the NP visually by excitation with UV or X-ray radiation or activate green or red photon-catalyzed reactions. The mesoporous shell has the advantages of a modular silica surface and accessible silane chemistry while also being able to host a variety of small molecules that could be of use in an RT agent. The synthesis of each of these components started with various literature preparations that were optimized or otherwise adapted to produce the presented final products. When attaching the biocompatible polymer PEG to the surface of the silica in this synthesis as well as the Bi NPs synthesis, common orthodoxy in these silane reactions was analyzed. While aprotic solvents and weak bases are the most common conditions for

producing a monolayer coating, conditions with stronger bases and aqueous reactions proved to produce a greater layer of polymer on the surface which is more ideal for its opsonization suppression application.

When assessed at an RT enhancer, the CaF_2-MS-PEG NPs performed well and were able to multiply the production of radicals throughout irradiation, resulting in measurable enhancements of cell killing. The NPs were notably non-cytotoxic in the absence of radiation, which allowed for a high dose of NPs to be applied. This enhancement, however, was variable and did not correlate with NP dose, in a way that suggests a more complicated enhancement mechanism than intended. The attempt to convert the platform to a photodynamic therapy agent has not yet been successful. Preliminary attempts to load Rose Bengal into the MS electrostatically were initially successful, but singlet oxygen generation was not observed in the system as hypothesized. Hydroxyl radical production increased with the addition of Rose Bengal, however, this did not improve the efficiency of the system enough to make up for the cytotoxicity inherent to having the dye present.

Future improvements to the CaF_2-MS NP system could be done in two ways, improving the biodistribution of the NPs and successfully integrating the photosensitizer. Surface treatments to improve the biodistribution of the NP will be similar to those suggested for the Bi NPs, including targeting ligands that could improve the accumulation of the NPs in specific types of affected sites. An equally complicated matter would be attaching the Rose Bengal to the NP such that photodynamic therapy is viable. This attachment would likely be covalent, perhaps by incorporating aminosilanes into the MS formation step to provide aminated surfaces in the pores. This functional group could then

be used for an EDC/NHS attachment strategy to RB's carboxylate group. This type of attachment would likely lead to a greater concentration of RB in the pore of the MS and would be effective if this bonding did not negatively affect the Rose Bengal's singlet oxygen-producing properties. Another detail of this alteration is that the amine on the surface of the NP should not be detrimental to the attachment of PEG. Whether this route or some other is taken, the ideal photodynamic therapy agent is a complex synthetic challenge which can be built upon the synthesis and assessment of the CaF_2 NPs in this work.

REFERENCES

(1)   Pan, H. Y.; Haffty, B. G.; Falit, B. P.; Buchholz, T. A.; Wilson, L. D.; Hahn, S. M.; Smith, B. D. Supply and Demand for Radiation Oncology in the United States: Updated Projections for 2015 to 2025. *Int. J. Radiat. Oncol.* **2016**, *96* (3), 493–500. https://doi.org/10.1016/J.IJROBP.2016.02.064.

(2)   Veldeman, L.; Madani, I.; Hulstaert, F.; De Meerleer, G.; Mareel, M.; De Neve, W. Evidence behind Use of Intensity-Modulated Radiotherapy: A Systematic Review of Comparative Clinical Studies. *Lancet Oncol.* **2008**, *9* (4), 367–375. https://doi.org/10.1016/S1470-2045(08)70098-6.

(3)   Burt, L. M.; Ying, J.; Poppe, M. M.; Suneja, G.; Gaffney, D. K. Risk of Secondary Malignancies after Radiation Therapy for Breast Cancer: Comprehensive Results. *Breast* **2017**, *35*, 122–129. https://doi.org/10.1016/j.breast.2017.07.004.

(4)   Warschkow, R.; Güller, U.; Cerny, T.; Schmied, B. M.; Plasswilm, L.; Putora, P. M. Secondary Malignancies after Rectal Cancer Resection with and without Radiation Therapy: A Propensity-Adjusted, Population-Based SEER Analysis. *Radiother. Oncol.* **2017**, *123* (1), 139–146. https://doi.org/10.1016/j.radonc.2017.02.007.

(5)   Ng, J.; Shuryak, I. Minimizing Second Cancer Risk Following Radiotherapy: Current Perspectives. *Cancer Manag. Res.* **2015**, *7*, 1–11. https://doi.org/10.2147/CMAR.S47220.

(6)   Turner, J. E.; Magee, J. L.; Wright, H. A.; Chatterjee, A.; Hamm, R. N.; Ritchie, R. H. Physical and Chemical Development of Electron Tracks in Liquid Water. *Radiat.*

Res. **1983**, *96* (3), 437. https://doi.org/10.2307/3576111.

(7)   Carter, J. D.; Cheng, N. N.; Qu, Y.; Suarez, G. D.; Guo, T. Nanoscale Energy Deposition by X-Ray Absorbing Nanostructures. *J. Phys. Chem. B* **2007**, *111* (40), 11622–11625. https://doi.org/10.1021/jp075253u.

(8)   Butterworth, K. T.; McMahon, S. J.; Currell, F. J.; Prise, K. M. Physical Basis and Biological Mechanisms of Gold Nanoparticle Radiosensitization. *Nanoscale* **2012**, *4* (16), 4830. https://doi.org/10.1039/c2nr31227a.

(9)   Stowell, C. A.; Korgel, B. A. Iridium Nanocrystal Synthesis and Surface Coating-Dependent Catalytic Activity. *Nano Lett.* **2005**, *5* (7), 1203–1207. https://doi.org/10.1021/nl050648f.

(10)   Schöttle, C.; Bockstaller, P.; Gerthsen, D.; Feldmann, C. Tungsten Nanoparticles from Liquid-Ammonia-Based Synthesis. *Chem. Commun.* **2014**, *50* (35), 4547–4550. https://doi.org/10.1039/c3cc49854a.

(11)   Sahoo, P. K.; Kalyan Kamal, S. S.; Premkumar, M.; Jagadeesh Kumar, T.; Sreedhar, B.; Singh, A. K.; Srivastava, S. K.; Chandra Sekhar, K. Synthesis of Tungsten Nanoparticles by Solvothermal Decomposition of Tungsten Hexacarbonyl. *Int. J. Refract. Met. Hard Mater.* **2009**, *27* (4), 784–791. https://doi.org/10.1016/j.ijrmhm.2009.01.005.

(12)   De Jong, W. H.; Hagens, W. I.; Krystek, P.; Burger, M. C.; Sips, A. J. A. M.; Geertsma, R. E. Particle Size-Dependent Organ Distribution of Gold Nanoparticles after Intravenous Administration. *Biomaterials* **2008**, *29* (12), 1912–1919.

https://doi.org/10.1016/j.biomaterials.2007.12.037.

(13) Mirjolet, C.; Papa, A. L.; Créhange, G.; Raguin, O.; Seignez, C.; Paul, C.; Truc, G.; Maingon, P.; Millot, N. The Radiosensitization Effect of Titanate Nanotubes as a New Tool in Radiation Therapy for Glioblastoma: A Proof-of-Concept. *Radiother. Oncol.* **2013**, *108* (1), 136–142. https://doi.org/10.1016/j.radonc.2013.04.004.

(14) Chen, X.; Shen, S.; Guo, L.; Mao, S. S. Semiconductor-Based Photocatalytic Hydrogen Generation. *Chem. Rev.* **2010**. https://doi.org/10.1021/cr1001645.

(15) Lehman, S. E.; Morris, A. S.; Mueller, P. S.; Salem, A. K.; Grassian, V. H.; Larsen, S. C. Silica Nanoparticle-Generated ROS as a Predictor of Cellular Toxicity: Mechanistic Insights and Safety by Design. *Environ. Sci. Nano* **2016**, *3* (1), 56–66. https://doi.org/10.1039/C5EN00179J.

(16) Longmire, M.; Choyke, P. L.; Kobayashi, H. Clearance Properties of Nano-Sized Particles and Molecules as Imagin Agents: Consideration and Caveats. *Nanomedicine (Lond)* **2008**, *3* (5), 703–717. https://doi.org/10.2217/17435889.3.5.703.Clearance.

(17) Narayanasamy, J.; Kubicki, J. D. Mechanism of Hydroxyl Radical Generation from a Silica Surface: Molecular Orbital Calculations. *J. Phys. Chem. B* **2005**, *109* (46), 21796–21807. https://doi.org/10.1021/jp0543025.

(18) Hainfeld, J. F.; Slatkin, D. N.; Smilowitz, H. M. The Use of Gold Nanoparticles to Enhance Radiotherapy in Mice. *Phys. Med. Biol.* **2004**, *49* (18), N309–N315. https://doi.org/10.1088/0031-9155/49/18/N03.

(19) Hainfeld, J. F.; Ridwan, S. M.; Stanishevskiy, Y.; Panchal, R.; Slatkin, D. N.; Smilowitz, H. M. Iodine Nanoparticles Enhance Radiotherapy of Intracerebral Human Glioma in Mice and Increase Efficacy of Chemotherapy. *Sci. Rep.* **2019**, *9* (1), 1–12. https://doi.org/10.1038/s41598-019-41174-5.

(20) Yu, X.; Li, A.; Zhao, C.; Yang, K.; Chen, X.; Li, W. Ultrasmall Semimetal Nanoparticles of Bismuth for Dual-Modal Computed Tomography/Photoacoustic Imaging and Synergistic Thermoradiotherapy. *ACS Nano* **2017**, *11* (4), 3990–4001. https://doi.org/10.1021/acsnano.7b00476.

(21) Tang, an; Hu, J.; Elmenoufy, A. H.; Yang, X. Highly Efficient FRET System Capable of Deep Photodynamic Therapy Established on X-ray Excited Mesoporous LaF 3 :Tb Scintillating Nanoparticles. https://doi.org/10.1021/acsami.5b03067.

(22) Chen, H.; Wang, G. D.; Chuang, Y. J.; Zhen, Z.; Chen, X.; Biddinger, P.; Hao, Z.; Liu, F.; Shen, B.; Pan, Z.; Xie, J. Nanoscintillator-Mediated X-Ray Inducible Photodynamic Therapy for in Vivo Cancer Treatment. *Nano Lett.* **2015**, *15* (4), 2249–2256. https://doi.org/10.1021/nl504044p.

(23) Wang, F.; Richards, V. N.; Shields, S. P.; Buhro, W. E. Kinetics and Mechanisms of Aggregative Nanocrystal Growth. *Chem. Mater.* **2014**, *26* (1), 5–21. https://doi.org/10.1021/cm402139r.

(24) Wu, Z.; Yang, S.; Wu, W. Shape Control of Inorganic Nanoparticles from Solution. *Nanoscale* **2016**, *8* (3), 1237–1259. https://doi.org/10.1039/C5NR07681A.

(25) Sugimoto, T. Underlying Mechanisms in Size Control of Uniform Nanoparticles. *J.*

Colloid Interface Sci. **2007**, *309* (1), 106–118. https://doi.org/10.1016/j.jcis.2007.01.036.

(26) Takahashi, K.; Yokoyama, S.; Matsumoto, T.; Cuya Huaman, J. L.; Kaneko, H.; Piquemal, J.-Y.; Miyamura, H.; Balachandran, J. Towards a Designed Synthesis of Metallic Nanoparticles in Polyols – Elucidation of the Redox Scheme in a Cobalt–Ethylene Glycol System. *New J. Chem.* **2016**, *40* (10), 8632–8642. https://doi.org/10.1039/C6NJ01738J.

(27) Wang, Y.; Xia, Y. Bottom-up and Top-down Approaches to the Synthesis of Monodispersed Spherical Colloids of Low Melting-Point Metals. *Nano Lett.* **2004**, *4* (10), 2047–2050. https://doi.org/10.1021/nl048689j.

(28) He, M.; Protesescu, L.; Caputo, R.; Krumeich, F.; Kovalenko, M. V. A General Synthesis Strategy for Monodisperse Metallic and Metalloid Nanoparticles (In, Ga, Bi, Sb, Zn, Cu, Sn, and Their Alloys) via in Situ Formed Metal Long-Chain Amides. *Chem. Mater.* **2015**, *27* (2), 635–647. https://doi.org/10.1021/cm5045144.

(29) Wang, F.; Tang, R.; Yu, H.; Gibbons, P. C.; Buhro, W. E. Size- and Shape-Controlled Synthesis of Bismuth Nanoparticles. *Chem. Mater.* **2008**, *20* (11), 3656–3662. https://doi.org/10.1021/cm8004425.

(30) Yarema, M.; Caputo, R.; Kovalenko, M. V. Precision Synthesis of Colloidal Inorganic Nanocrystals Using Metal and Metalloid Amides. *Nanoscale* **2013**, *5* (18), 8398. https://doi.org/10.1039/c3nr02076b.

(31) Carmalt, C. J.; Compton, N. A.; Errington, R. J.; Fisher, G. A.; Moenander, I.;

Norman, N. C.; Whimire, K. H. Homoleptic Bismuth Amides. *Inorg. Synth. Vol. 37* **1997**, *31*, 98–101. https://doi.org/10.1002/9780470132623.ch15.

(32) Horváth, O.; Mikó, I. Spectra, Equilibrium and Photoredox Chemistry of Iodobismuthate(III) Complexes in Acetonitrile. *Inorganica Chim. Acta* **2000**, *304* (2), 210–218. https://doi.org/10.1016/S0020-1693(00)00090-6.

(33) Greenwood, N. N.; Earnshaw, A. *Chemistry of the Elements*, 2nd ed.; Elsevier: Oxford, 1995; Vol. 2. https://doi.org/10.1016/S0277-5387(00)84180-7.

(34) Pandurangappa, C.; Lakshminarasappa, B. N.; Nagabhushana, B. M. Synthesis and Characterization of CaF2 Nanocrystals. *J. Alloys Compd.* **2010**, *489* (2), 592–595. https://doi.org/10.1016/j.jallcom.2009.09.118.

(35) Wang, F.; Fan, X.; Pi, D.; Wang, M. Synthesis and Luminescence Behavior of Eu3+-Doped CaF2 Nanoparticles. *Solid State Commun.* **2005**, *133* (12), 775–779. https://doi.org/10.1016/J.SSC.2005.01.014.

(36) Song, L.; Gao, J.; Li, J. Sensitized Luminescence of Water-Dispersible CaF2: RE 3+ (RE=Eu, Tb, Ce/Tb) Nanoparticles through Surfactant Coating Ligands. *J. Lumin.* **2014**, *151*, 18–21. https://doi.org/10.1016/j.jlumin.2014.01.076.

(37) Pedroni, M.; Piccinelli, F.; Passuello, T.; Giarola, M.; Mariotto, G.; Polizzi, S.; Bettinelli, M.; Speghini, A. Lanthanide Doped Upconverting Colloidal CaF2 Nanoparticles Prepared by a Single-Step Hydrothermal Method: Toward Efficient Materials with near Infrared-to-near Infrared Upconversion Emission. *Nanoscale* **2011**, *3* (4), 1456–1460. https://doi.org/10.1039/c0nr00860e.

(38)   Zahedifar, M.; Sadeghi, E.; Shanei, M. M.; Sazgarnia, A.; Mehrabi, M. Afterglow Properties of CaF2:Tm Nanoparticles and Its Potential Application in Photodynamic Therapy. *J. Lumin.* **2016**, *171*, 254–258. https://doi.org/10.1016/j.jlumin.2015.11.043.

(39)   Cortelletti, P.; Facciotti, C.; Cantarelli, I. X.; Canton, P.; Quintanilla, M.; Vetrone, F.; Speghini, A.; Pedroni, M. Nd3+ Activated CaF2 NPs as Colloidal Nanothermometers in the Biological Window. *Opt. Mater. (Amst).* **2017**, *68*, 29–34. https://doi.org/10.1016/j.optmat.2016.11.019.

(40)   Cortelletti, P.; Pedroni, M.; Boschi, F.; Pin, S.; Ghigna, P.; Canton, P.; Vetrone, F.; Speghini, A. Luminescence of Eu3+ Activated CaF2 and SrF2 Nanoparticles: Effect of the Particle Size and Codoping with Alkaline Ions. *Cryst. Growth Des.* **2018**, *18* (2), 686–694. https://doi.org/10.1021/acs.cgd.7b01050.

(41)   Dexter, D. L. A Theory of Sensitized Luminescence in Solids. *J. Chem. Phys.* **1953**, *21* (5), 836–850. https://doi.org/10.1063/1.1699044.

(42)   Dexter, D. L.; Schulman, J. H. Theory of Concentration Quenching in Inorganic Phosphors. *J. Chem. Phys.* **1954**, *22* (6), 1063–1070. https://doi.org/10.1063/1.1740265.

(43)   Sahare, P. D.; Singh, M.; Kumar, P. Effect of Annealing and Impurity Concentration on the TL Characteristics of Nanocrystalline Mn-Doped CaF2. *Radiat. Meas.* **2015**, *80*, 29–37. https://doi.org/10.1016/j.radmeas.2015.07.003.

(44)   Möller, K.; Bein, T. Talented Mesoporous Silica Nanoparticles. *Chem. Mater.* **2017**,

29 (1), 371–388. https://doi.org/10.1021/acs.chemmater.6b03629.

(45)   Guerrero-Martínez, A.; Pérez-Juste, J.; Liz-Marzán, L. M. Recent Progress on Silica

Coating of Nanoparticles and Related Nanomaterials. *Adv. Mater.* **2010**, *22* (11),

1182–1195. https://doi.org/10.1002/adma.200901263.

(46)   Chen, Y.; Chen, H.; Guo, L.; He, Q.; Chen, F.; Zhou, J.; Feng, J.; Shi, J.

Hollow/Rattle-Type Mesoporous Nanostructures by a Structural Difference-Based

Selective   Etching   Strategy.   *ACS   Nano*   **2010**,   *4*   (1),   529–539.

https://doi.org/10.1021/nn901398j.

(47)   Xu, Q.; Ensign, L. M.; Boylan, N. J.; Schön, A.; Gong, X.; Yang, J. C.; Lamb, N.

W.; Cai, S.; Yu, T.; Freire, E.; Hanes, J. Impact of Surface Polyethylene Glycol

(PEG) Density on Biodegradable Nanoparticle Transport in Mucus Ex Vivo and

Distribution   in   Vivo.   *ACS   Nano*   **2015**,   *9*   (9),   9217–9227.

https://doi.org/10.1021/acsnano.5b03876.

(48)   Gref, R.; Lück, M.; Quellec, P.; Marchand, M.; Dellacherie, E.; Harnisch, S.; Blunk,

T.; Müller, R. H. "Stealth" Corona-Core Nanoparticles Surface Modified by

Polyethylene Glycol (PEG): Influences of the Corona (PEG Chain Length and

Surface Density) and of the Core Composition on Phagocytic Uptake and Plasma

Protein Adsorption. *Colloids Surfaces B Biointerfaces* **2000**, *18* (3–4), 301–313.

https://doi.org/10.1016/S0927-7765(99)00156-3.

(49)   Perry, J. L.; Reuter, K. G.; Kai, M. P.; Herlihy, K. P.; Jones, S. W.; Luft, J. C.;

Napier, M.; Bear, J. E.; Desimone, J. M. PEGylated PRINT Nanoparticles: The

Impact of PEG Density on Protein Binding, Macrophage Association, Biodistribution, and Pharmacokinetics. *Nano Lett.* **2012**, *12* (10), 5304–5310. https://doi.org/10.1021/nl302638g.

(50)   Owens, D. E.; Peppas, N. A. Opsonization, Biodistribution, and Pharmacokinetics of Polymeric Nanoparticles. *Int. J. Pharm.* **2006**, *307* (1), 93–102. https://doi.org/10.1016/j.ijpharm.2005.10.010.

(51)   Li, S. D.; Huang, L. Stealth Nanoparticles: High Density but Sheddable PEG Is a Key for Tumor Targeting. *J. Control. Release* **2010**, *145* (3), 178–181. https://doi.org/10.1016/j.jconrel.2010.03.016.

(52)   Zhu, M.; Lerum, M. Z.; Chen, W. How to Prepare Reproducible, Homogeneous, and Hydrolytically Stable Aminosilane-Derived Layers on Silica. *Langmuir* **2012**, *28* (1), 416–423. https://doi.org/10.1021/la203638g.

(53)   Dong, N. N.; Pedroni, M.; Piccinelli, F.; Conti, G.; Sbarbati, A.; Ramírez-Hernández, J. E.; Maestro, L. M.; Iglesias-De La Cruz, M. C.; Sanz-Rodriguez, F.; Juarranz, A.; Chen, F.; Vetrone, F.; Capobianco, J. A.; Solé, J. G.; Bettinelli, M.; Jaque, D.; Speghini, A. NIR-to-NIR Two-Photon Excited CaF2:Tm3+,Yb 3+ Nanoparticles: Multifunctional Nanoprobes for Highly Penetrating Fluorescence Bio-Imaging. *ACS Nano* **2011**, *5* (11), 8665–8671. https://doi.org/10.1021/nn202490m.

(54)   Sasidharan, S.; Jayasree, A.; Fazal, S.; Koyakutty, M.; Nair, S. V.; Menon, D. Ambient Temperature Synthesis of Citrate Stabilized and Biofunctionalized,

Fluorescent Calcium Fluoride Nanocrystals for Targeted Labeling of Cancer Cells. *Biomater. Sci.* **2013**, *1* (3), 294–305. https://doi.org/10.1039/c2bm00127f.

(55)   Portioli, C.; Pedroni, M.; Benati, D.; Donini, M.; Bonafede, R.; Mariotti, R.; Perbellini, L.; Cerpelloni, M.; Dusi, S.; Speghini, A.; Bentivoglio, M. Citrate-Stabilized Lanthanide-Doped Nanoparticles: Brain Penetration and Interaction with Immune Cells and Neurons. *Nanomedicine* **2016**, *12* (23), 3039–3051. https://doi.org/10.2217/nnm-2016-0297.

(56)   Sun, C.; Pratx, G.; Carpenter, C. M.; Liu, H.; Cheng, Z.; Gambhir, S. S.; Xing, L. Synthesis and Radioluminescence of PEGylated Eu3+-Doped Nanophosphors as Bioimaging Probes. *Adv. Mater.* **2011**, *23* (24), H195–H199. https://doi.org/10.1002/adma.201100919.

(57)   Sudheendra, L.; Das, G. K.; Li, C.; Stark, D.; Cena, J.; Cherry, S.; Kennedy, I. M. NaGdF4:Eu3+ Nanoparticles for Enhanced X-Ray Excited Optical Imaging. *Chem. Mater.* **2014**, *26* (5), 1881–1888. https://doi.org/10.1021/cm404044n.

(58)   Bezerra, C. dos S.; Valerio, M. E. G. Structural and Optical Study of CaF2 Nanoparticles Produced by a Microwave-Assisted Hydrothermal Method. *Phys. B Condens. Matter* **2016**, *501*, 106–112. https://doi.org/10.1016/j.physb.2016.08.025.

(59)   Jacobsohn, L. G.; Sprinkle, K. B.; Roberts, S. A.; Kucera, C. J.; James, T. L.; Yukihara, E. G.; Devol, T. A.; Ballato, J. Fluoride Nanoscintillators. *J. Nanomater.* **2011**, *2011*. https://doi.org/10.1155/2011/523638.

(60)   Marrone, M. J. Radiation-Induced Luminescence in Silica Core Optical Fibers.

Appl. Phys. Lett. **1981**, *38* (3), 115–117. https://doi.org/10.1063/1.92294.

(61)   Bartolo, B.; Godberg, V.; Pacheco, D. *Luminescence of Inorganic Solids*; Springer US, 1978.

(62)   Danilkin, M. I.; Belousov, A. P.; Klimonskii, S. O.; Kuznetsov, V. D.; Lust, A. L.; Nikiforov, V. N.; Paama, L. N.; Pammo, I. K.; Seeman, V. O. Formation of Eu2+ and Eu3+ Centers in Synthesis of CaF2:Eu Luminophores. *J. Appl. Spectrosc.* **2007**, *74* (6), 858–865. https://doi.org/10.1007/s10812-007-0133-5.

(63)   Lehman, S. E.; Morris, A. S.; Mueller, P. S.; Salem, A. K.; Grassian, V. H.; Larsen, S. C. Silica Nanoparticle-Generated ROS as a Predictor of Cellular Toxicity: Mechanistic Insights and Safety by Design. *Environ. Sci. Nano* **2016**, *3* (1), 56–66. https://doi.org/10.1039/C5EN00179J.

(64)   Rózanowska, M.; Ciszewska, J.; Korytowski, W.; Sarna, T. Rose-Bengal-Photosensitized Formation of Hydrogen Peroxide and Hydroxyl Radicals. *J. Photochem. Photobiol. B Biol.* **1995**, *29* (1), 71–77. https://doi.org/10.1016/1011-1344(95)90259-7.

(65)   Alexis, F.; Pridgen, E.; Molnar, L. K.; Farokhzad, O. C. Factors Affecting the Clearance and Biodistribution of Polymeric Nanoparticles. *Mol. Pharm.* **2008**, *5* (4), 505–515. https://doi.org/10.1021/mp800051m.

(66)   Jaganathan, H.; Godin, B. Biocompatibility Assessment of Si-Based Nano- and Micro-Particles. *Adv. Drug Deliv. Rev.* **2012**, *64* (15), 1800–1819. https://doi.org/10.1016/j.addr.2012.05.008.

(67)   Pozzi, D.; Colapicchioni, V.; Caracciolo, G.; Piovesana, S.; Capriotti, A. L.; Palchetti, S.; De Grossi, S.; Riccioli, A.; Amenitsch, H.; Laganà, A. Effect of Polyethyleneglycol (PEG) Chain Length on the Bio-Nano-Interactions between PEGylated Lipid Nanoparticles and Biological Fluids: From Nanostructure to Uptake in Cancer Cells. *Nanoscale* **2014**, *6* (5), 2782–2792. https://doi.org/10.1039/c3nr05559k.